Supplementary Information for

General synthesis of neighboring dual-atomic sites with a specific pre-designed distance *via* an interfacial-fixing strategy

Yan Yan[1], Rui Yu[1], Mingkai Liu[*1], Zehua Qu[3], Jifeng Yang[1], Siyuan He[1], Hongliang Li[*2], Jie Zeng[*1,2]

[1]School of Chemistry & Chemical Engineering, Anhui University of Technology, Ma'anshan, Anhui 243002, P. R. China

[2]Hefei National Research Center for Physical Sciences at the Microscale, Key Laboratory of Strongly-Coupled Quantum Matter Physics of Chinese Academy of Sciences, Key Laboratory of Surface and Interface Chemistry and Energy Catalysis of Anhui Higher Education Institutes, Department of Chemical Physics, University of Science and Technology of China, Hefei, Anhui 230026, P. R. China

[3]State Key Laboratory of Molecular Engineering of Polymers, Department of Macromolecular Science, Fudan University, Shanghai 200433, China.

*e-mail: liumingkai@ahut.edu.cn; lihl@ustc.edu.cn; zengj@ustc.edu.cn

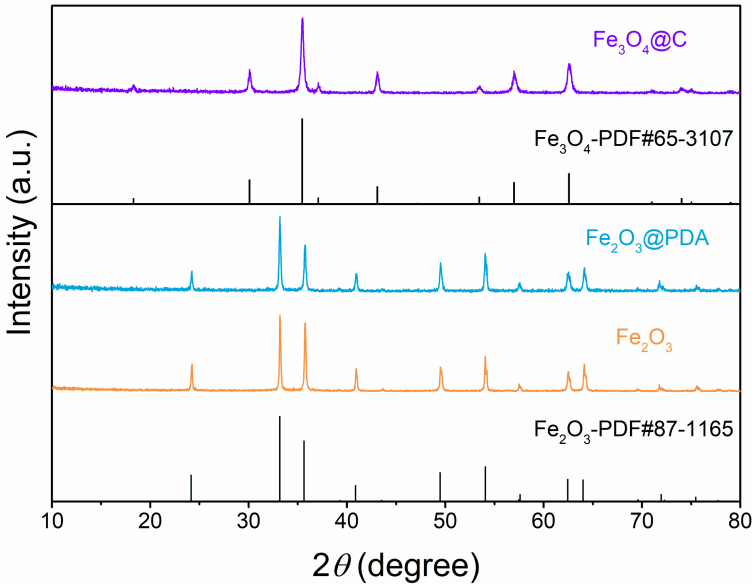

Supplementary Figure 1 | XRD patterns of Fe_2O_3, Fe_2O_3@PDA, and Fe_3O_4@C.

Note:

The absence of carbon peak, typically observed at around 26º, can be attributed to the strong diffraction peak of Fe_3O_4. The walls of the formed carbon tubes were too thin to produce noticeable diffraction peaks.

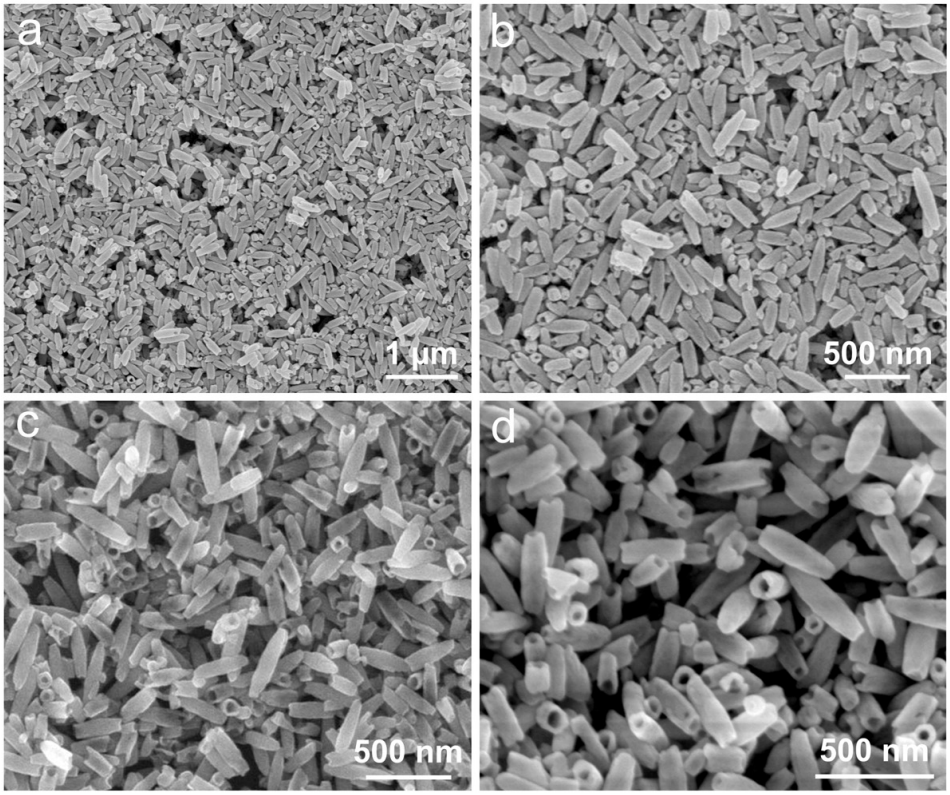

Supplementary Figure 2| Morphology characterizations of Fe_2O_3 hollow nanotubes. (**a-d**) SEM images of Fe_2O_3 hollow nanotubes at different magnifications.

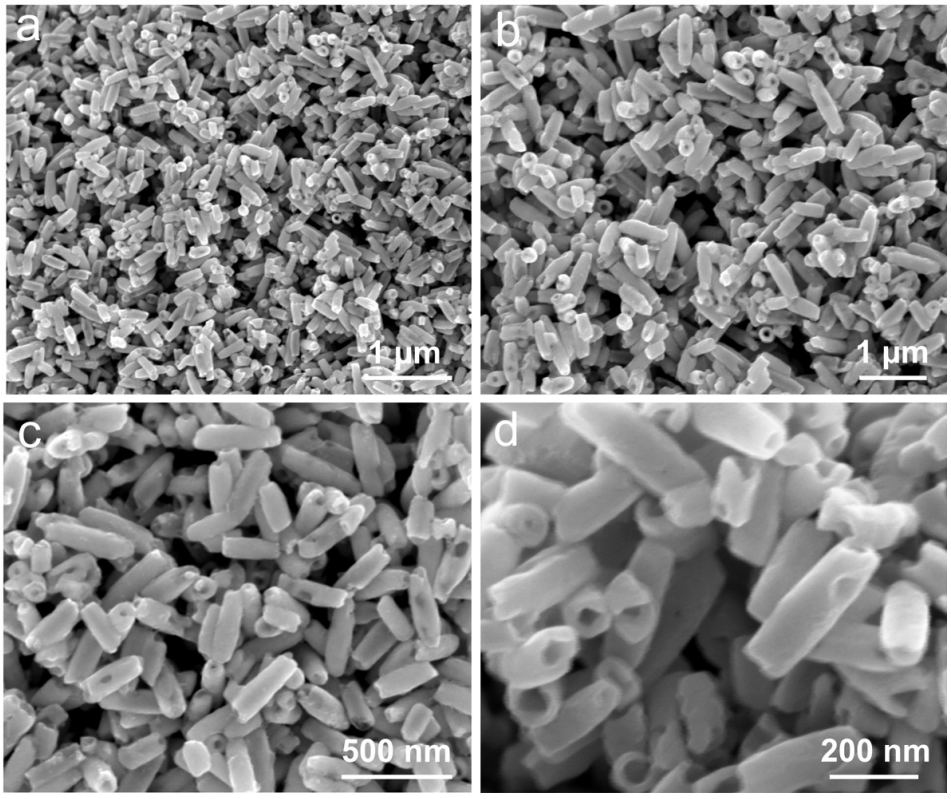

Supplementary Figure 3 | Morphology characterizations of Fe_2O_3@PDA hollow nanotubes. (**a-d**) SEM images of Fe_2O_3@PDA hollow nanotubes at different magnifications.

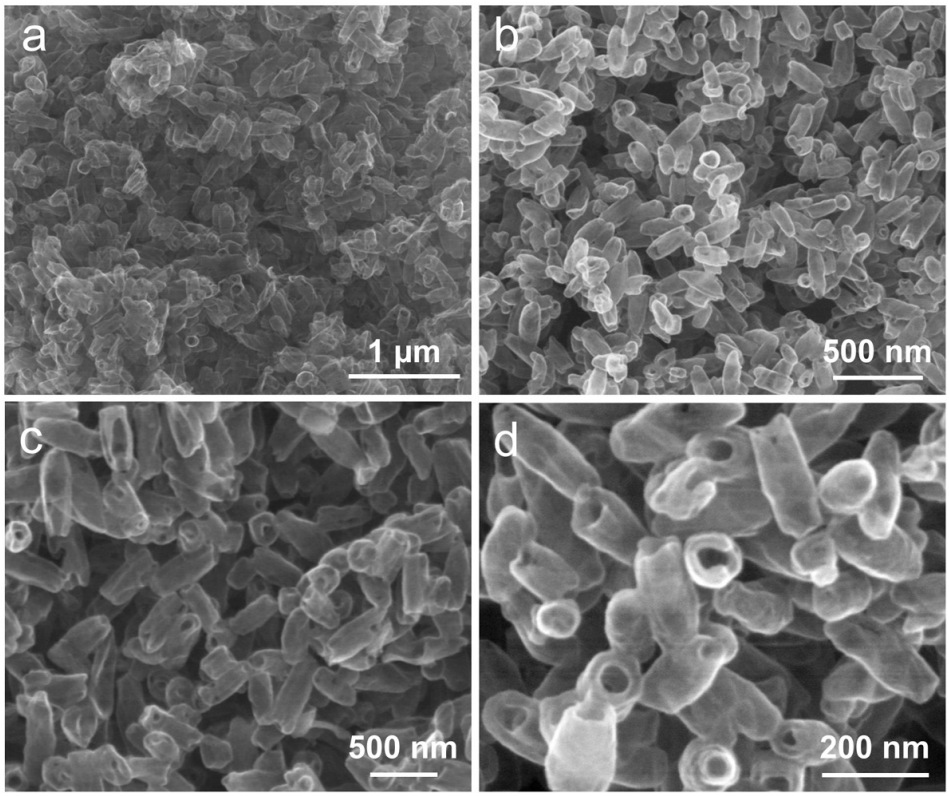

Supplementary Figure 4 | Morphology characterizations of Fe_2-N_6-containing hollow nanotubes. (**a-d**) SEM images of Fe_2-N_6-containing hollow nanotubes at different magnifications.

Supplementary Table S1 | Contents of N element in Fe_2-N_6 and Fe_1-N_4 before and after chemical etching.

Samples	Before etching	After etching
Fe_1-N_4	5.1 wt%	4.2 wt%
Fe_2-N_6	9.2 wt%	8.4 wt%

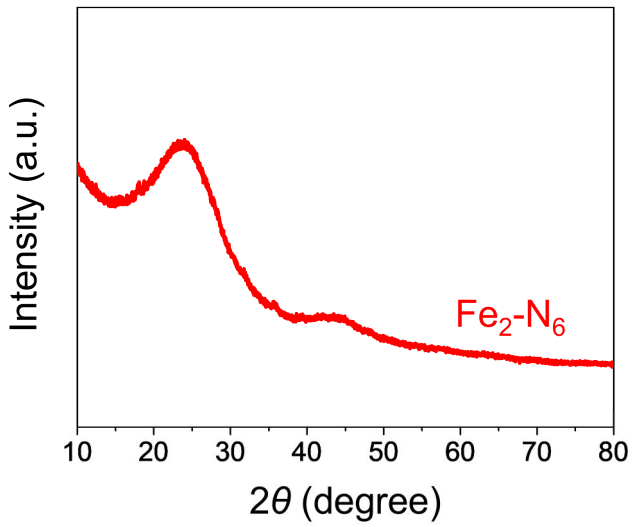

Supplementary Figure 5 | XRD patterns of Fe_2-N_6.

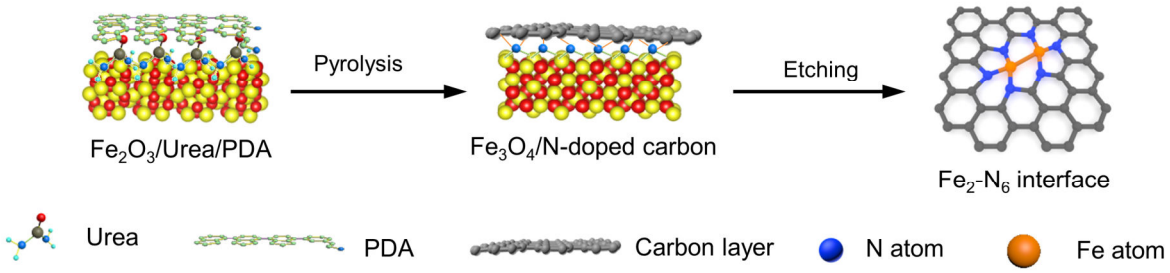

Supplementary Figure 6 | Schematic illustration of the conversion process from PDA+urea to N-doped carbon layers.

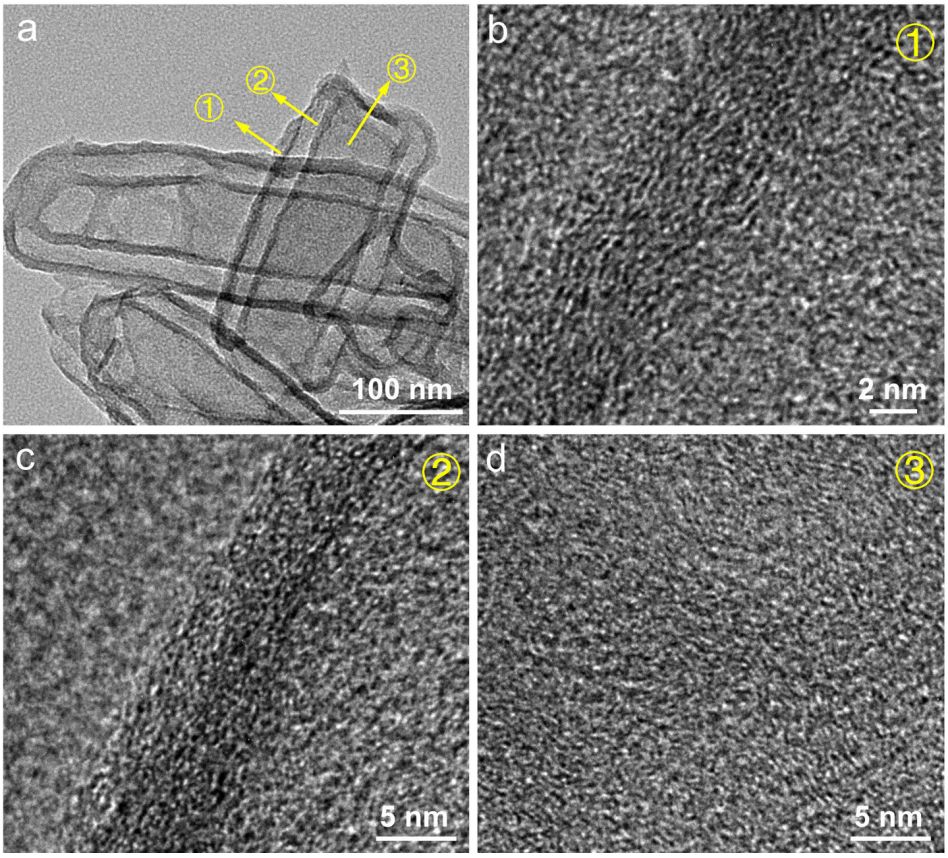

Supplementary Figure 7 | Structural characterizations of Fe_2-N_6. (**a**) TEM image of Fe_2-N_6-based hollow carbon nanotubes. (**b-d**) HRTEM images of the corresponding regions in panel a.

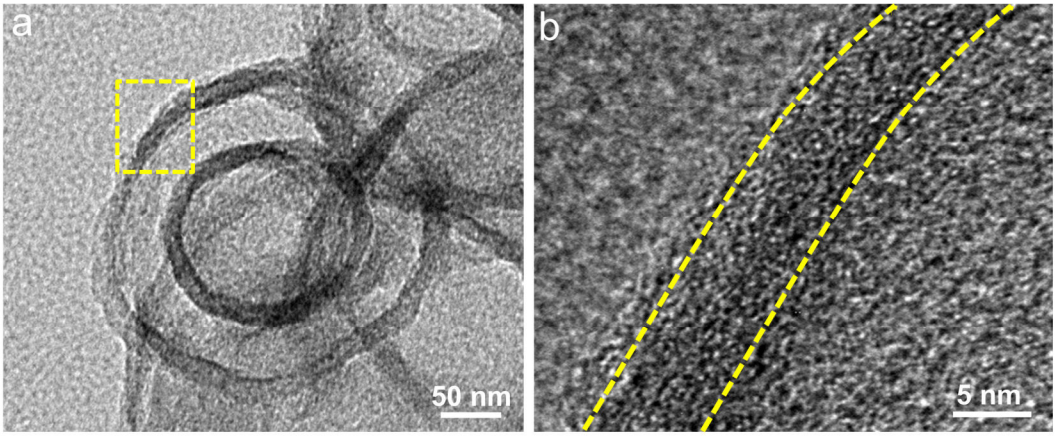

Supplementary Figure 8 | Structural characterizations of Fe_2-N_6. (**a**) TEM image of Fe_2-N_6 based hollow carbon nanotubes from the top view. (**b**) HRTEM image of the carbon layer marked in panel a.

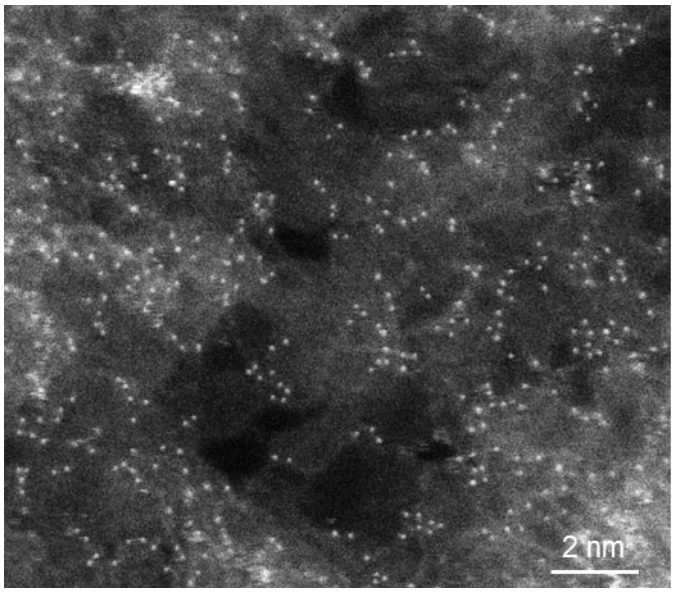

Supplementary Figure 9 | Structural characterizations of Fe_2-N_6. HAADF-STEM image of Fe_2-N_6 at low magnification.

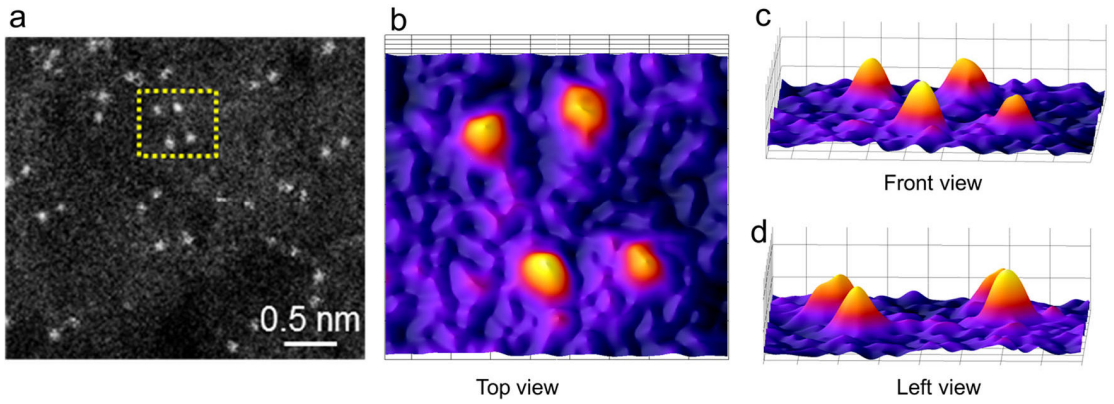

Supplementary Figure 10 | 3D atom-overlapping Gaussian-function fitting maps. (**a**) HAADF-STEM image of Fe atom pairs. (**b**) Top view, (**c**) front view, and (**d**) left view of the fitting maps.

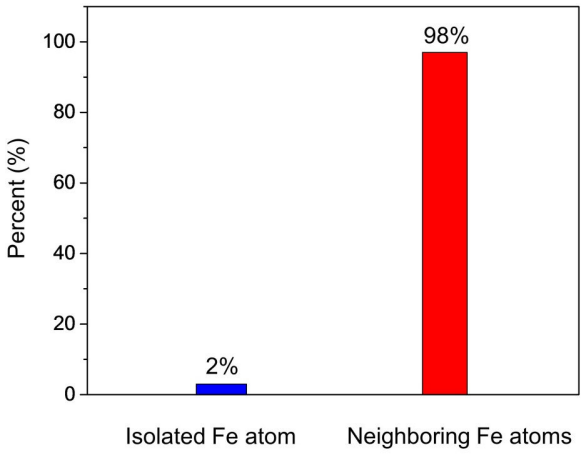

Supplementary Figure 11 | Distance distribution between neighboring Fe atoms. When measuring the distance between neighboring atoms, we counted only the closest ones based on one atom.

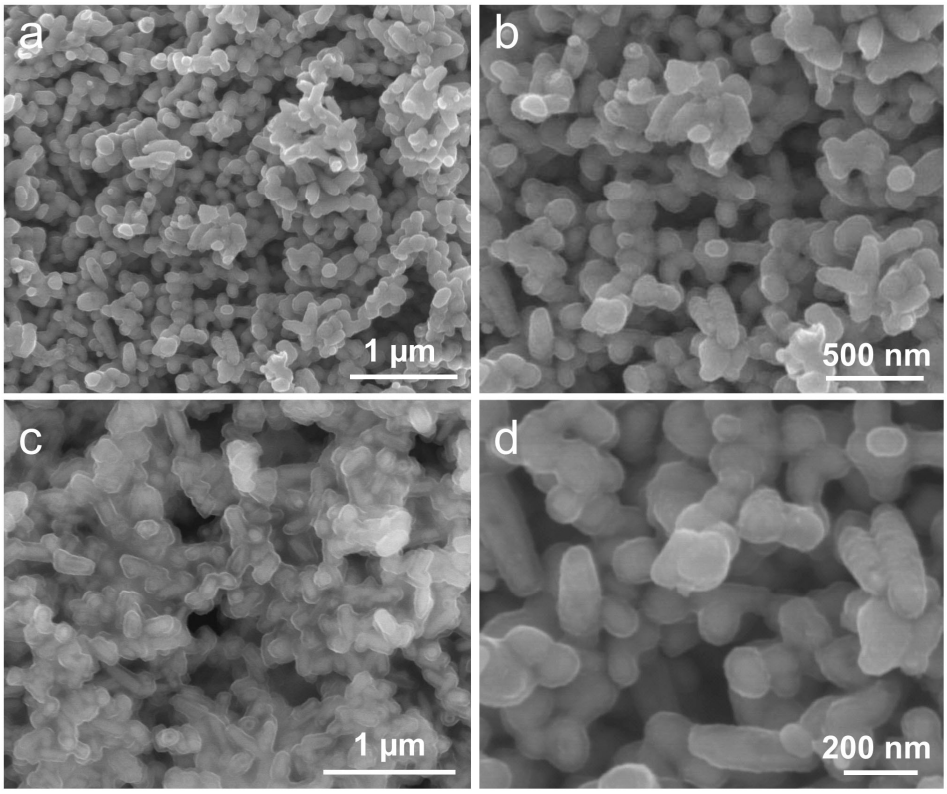

Supplementary Figure 12 | Morphology characterizations of Fe_2O_3/urea/PDA hollow nanotubes. (**a-d**) SEM images of Fe_2O_3/urea/PDA hollow nanotubes at different magnifications. This sample was prepared *via* using standard experimental procedures for Fe_2O_3@PDA hollow nanotubes except for applying double usage of PDA.

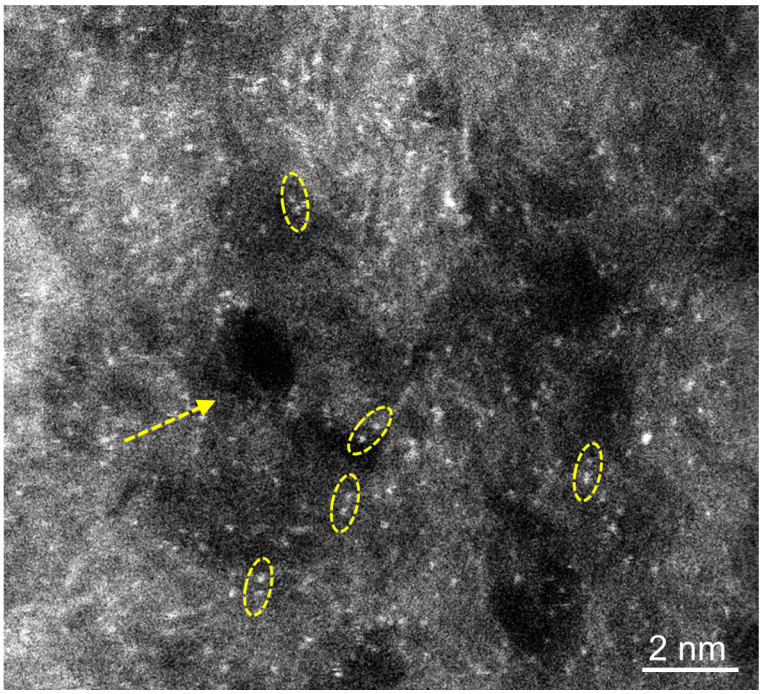

Supplementary Figure 13 | HAADF-STEM image of Fe_2-N_6 sample with thick carbon layers obtained from the double usage of PDA. An arrow is used to indicate the pores on the carbon layers. The ellipse shows the adjacently anchored Fe sites.

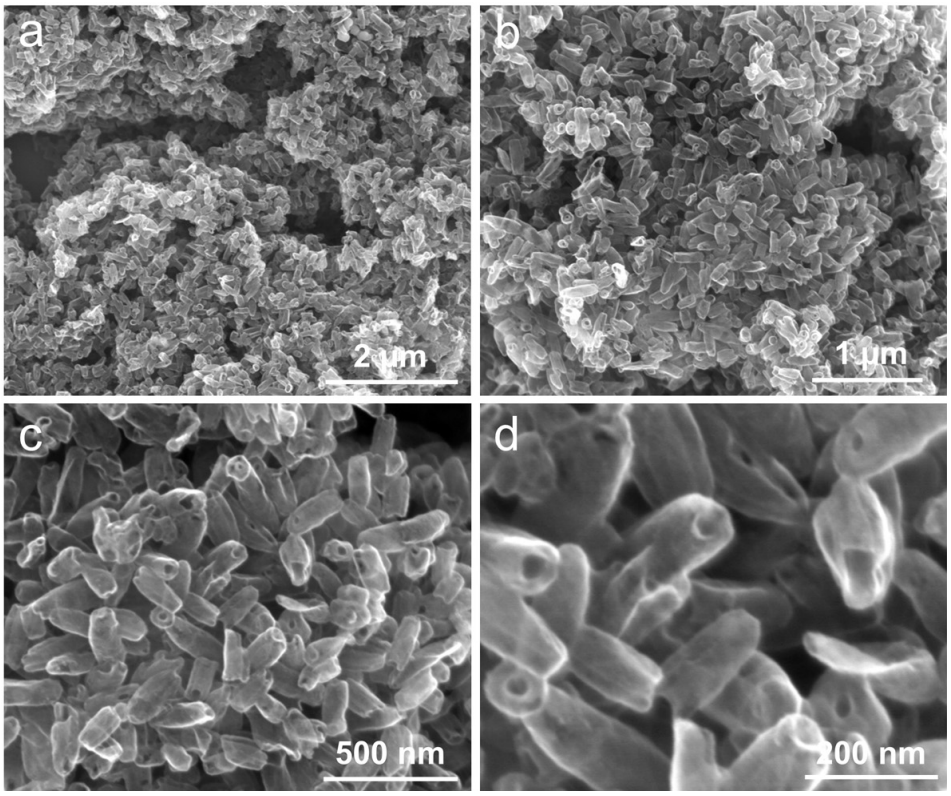

Supplementary Figure 14 | Morphology characterizations of Fe_1-N_4-containing hollow nanotubes. (**a-d**) SEM images of Fe_1-N_4-containing hollow nanotubes at different magnifications.

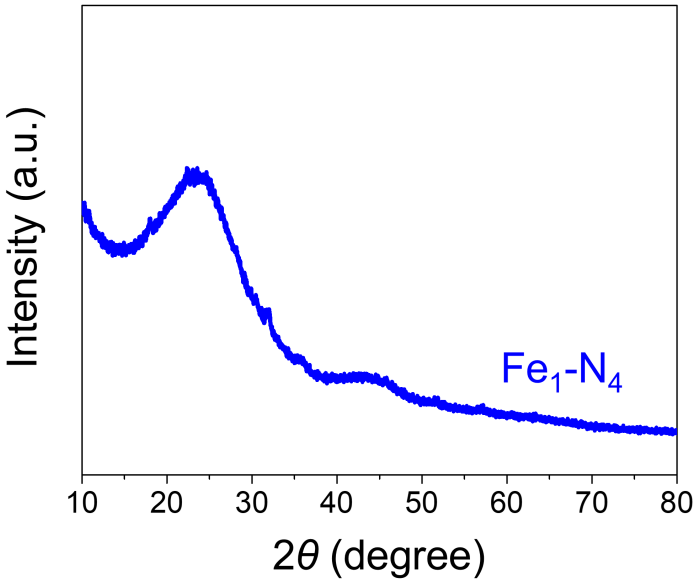

Supplementary Figure 15 | XRD patterns of Fe_1-N_4.

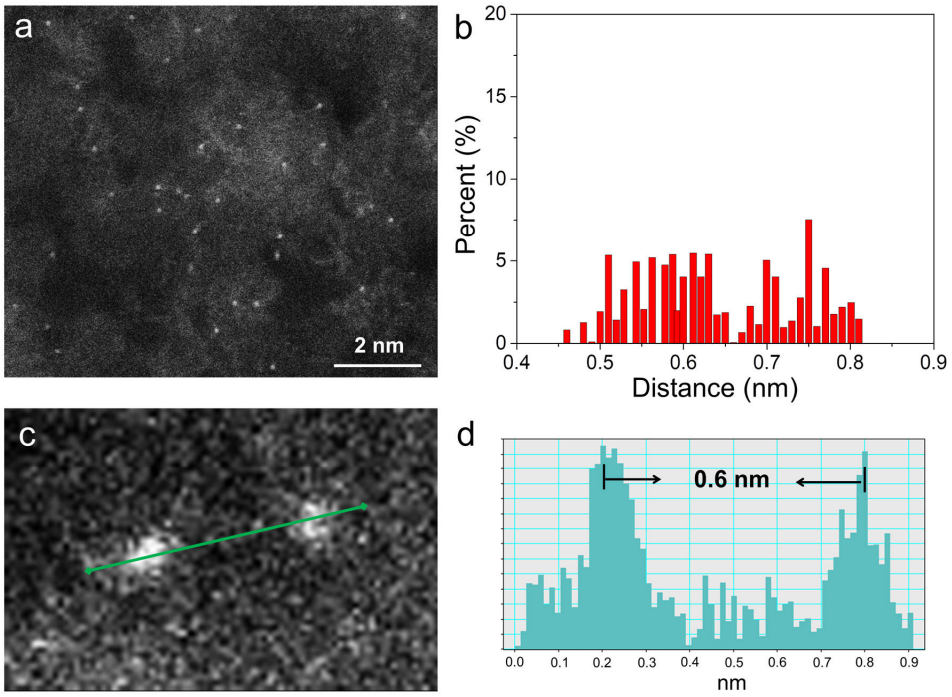

Supplementary Figure 16 | Characterizations of Fe_1-N_4. (**a**) HAADF-STEM image of Fe_1-N_4 and (**b**) the corresponding atomic distance distribution. (**c**) Enlarged HAADF-STEM image of the two atoms and (**d**) line-scanning intensity profiles obtained from the region in panel **c**.

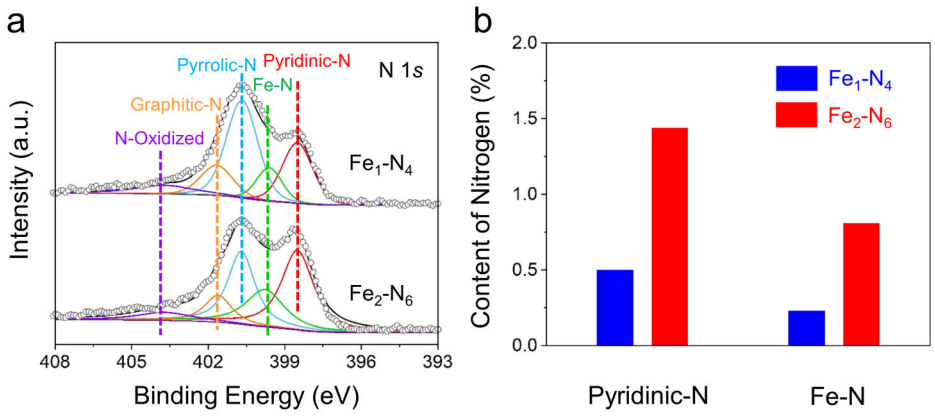

Supplementary Figure 17 | XPS characterizations of N 1*s* for Fe_1-N_4 and Fe_2-N_6. (**a**) High-resolution N 1*s* XPS spectra of Fe_1-N_4 and Fe_2-N_6 samples. (**b**) Contents of Pyridinic-N and Fe-N in Fe_1-N_4 and Fe_2-N_6.

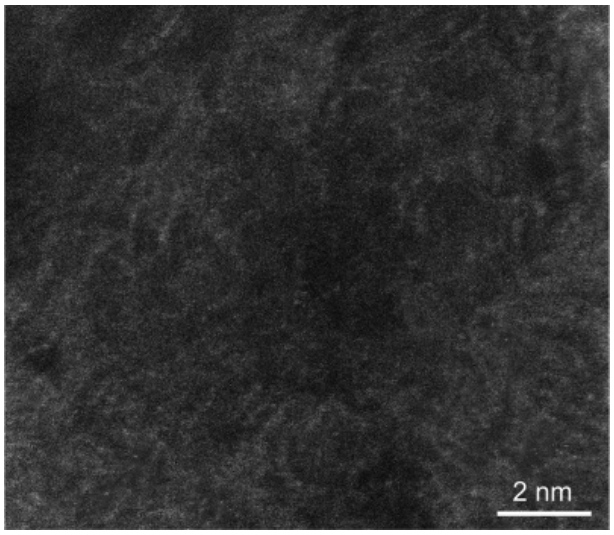

Supplementary Figure 18 | HAADF-STEM image of samples prepared based on the same procedure according to Fe_2-N_6 with Fe template substituting the Fe_3O_4 template.

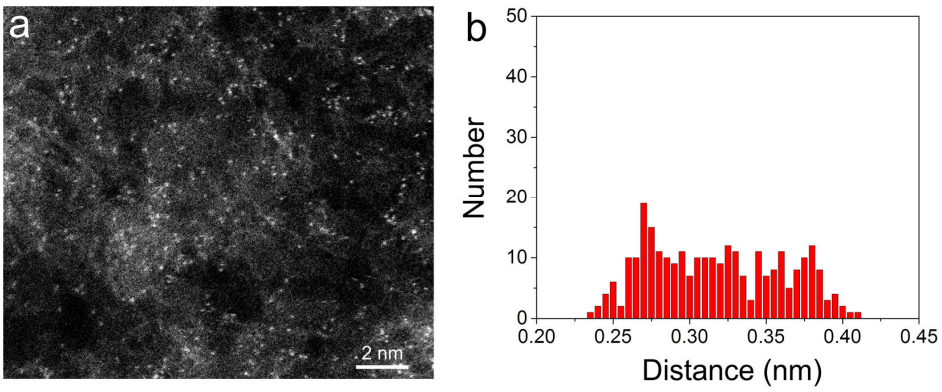

Supplementary Figure 19 | Characterizations of prepared Fe moiety with ligand of ethanediamine. (**a**) HAADF-STEM image of prepared Fe moiety with ligand of ethanediamine. (**b**) Distance distribution between adjacent Fe atoms.

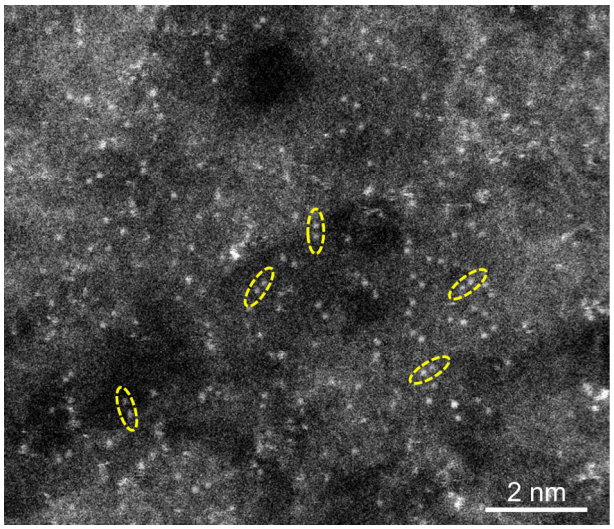

Supplementary Figure 20 | HAADF-STEM image of prepared Fe moiety with ligand of thiourea.

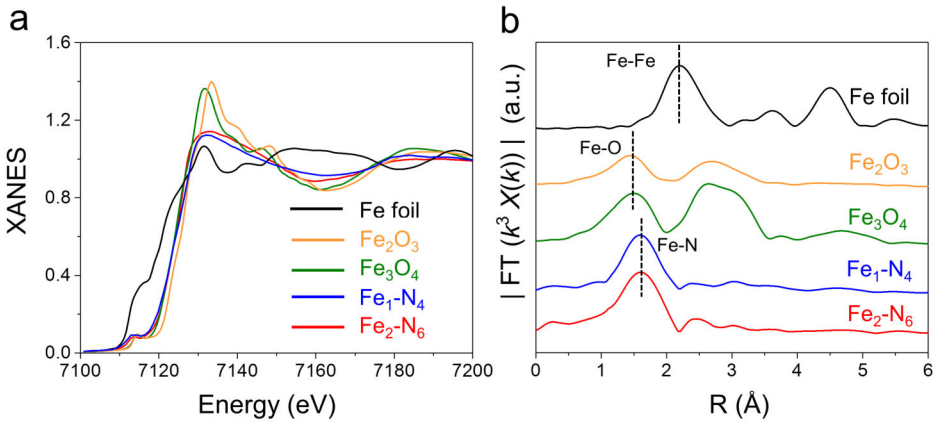

Supplementary Figure 21 | XAFS characterizations of Fe_1-N_4 and Fe_2-N_6. (**a**) Fe K-edge XANES spectra and (**b**) EXAFS spectra of Fe_1-N_4 and Fe_2-N_6. Fe foil, Fe_2O_3, and Fe_3O_4 were used as references.

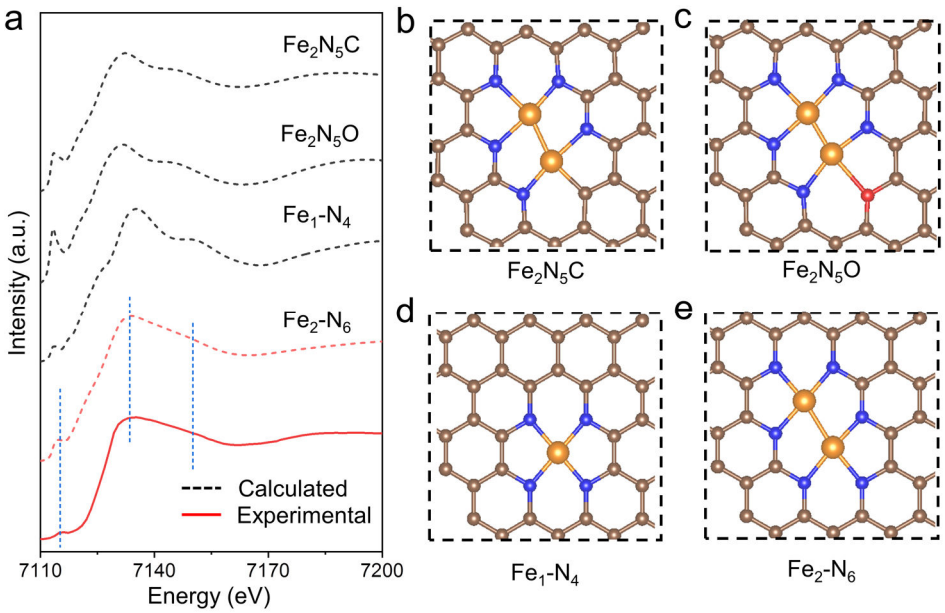

Supplementary Figure 22 | Calculated XANES spectra. (**a**) Experimental spectra of Fe_2-N_6 and calculated spectra of different structural models. The models of the calculated spectra are listed on the right. (**b-e**) Models of Fe_2-N_5C, Fe_2-N_5O, Fe-N_4, and Fe_2-N_6, respectively.

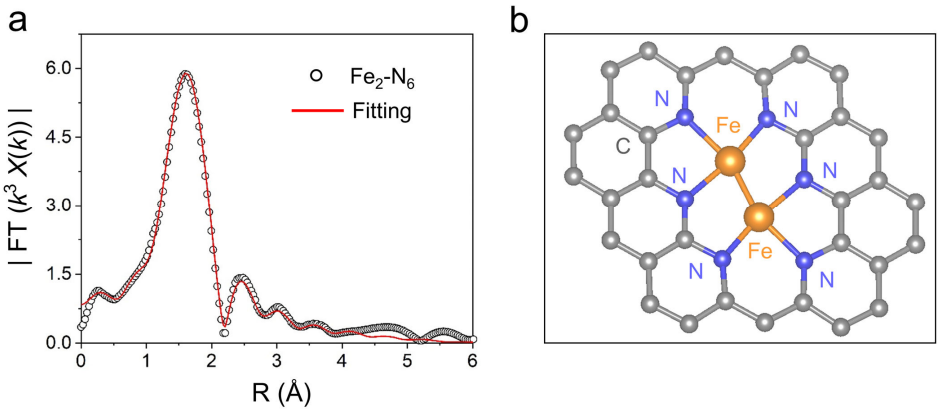

Supplementary Figure 23 | Identification of coordination structures of Fe_2-N_6. (**a**) EXAFS R-space fitting curve and (**b**) the corresponding configuration model for Fe_2-N_6. The gray, blue, and orange spheres represent C, N, and Fe atoms, respectively.

Supplementary Table 2. EXAFS data fitting results of Fe_2-N_6 and Fe_1-N_4, respectively.

Sample	Shell	*CN*[a]	*R* (Å)[b]	σ^2 (Å^2)[c]	ΔE_0 (eV)[d]	*R* factor (%)
Fe_2-N_6	Fe-N	2.8	1.90	0.010	3.062	0.0002
	Fe-Fe	0.9	2.62	0.014		
Fe_1-N_4	Fe-N	3.8	1.84	0.002	2.483	0.0005

[a]*CN*: coordination numbers; [b]*R*: bond distance; [c]σ^2: Debye-Waller factors; [d]ΔE_0: the inner potential correction. *R* factor: goodness of fit.

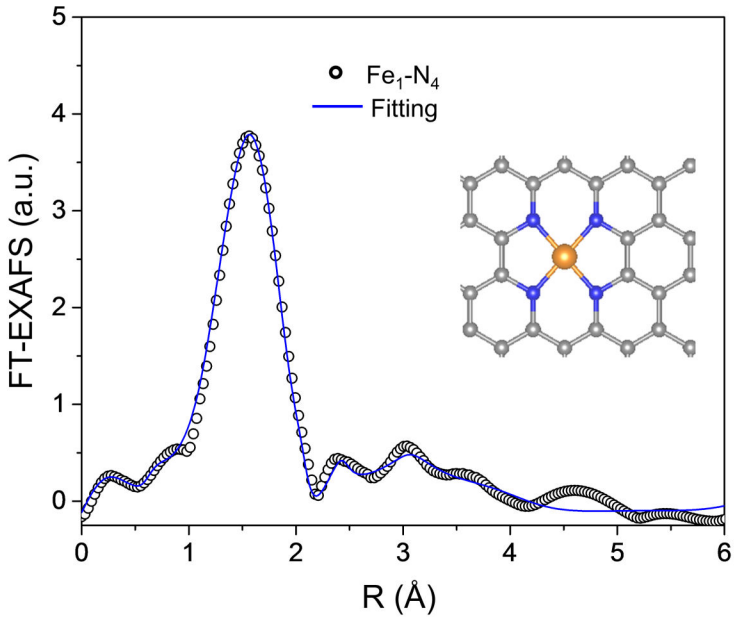

Supplementary Figure 24 | EXAFS R-space fitting curve and the corresponding configuration model for Fe_1-N_4. The gray, blue, and orange spheres represent C, N, and Fe atoms, respectively.

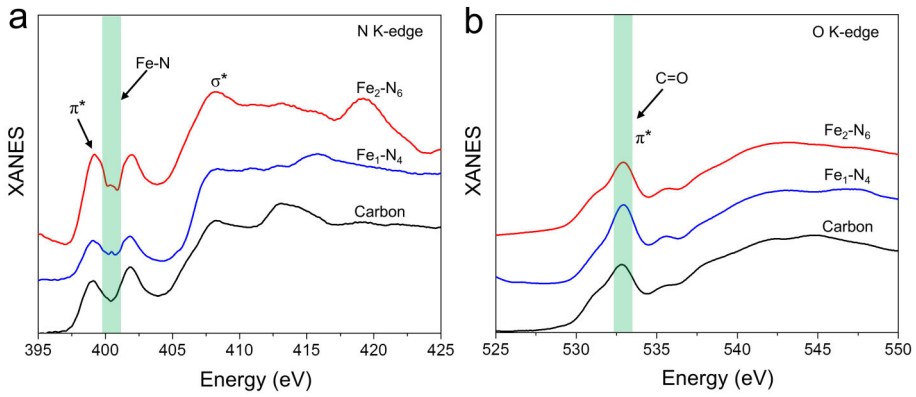

Supplementary Figure 25 | Soft XANES results of N and O K-edge spectra. (**a**) N K-edge and (**b**) O K-edge XANES spectra of Fe_2-N_6, Fe_1-N_4 and carbon matrix.

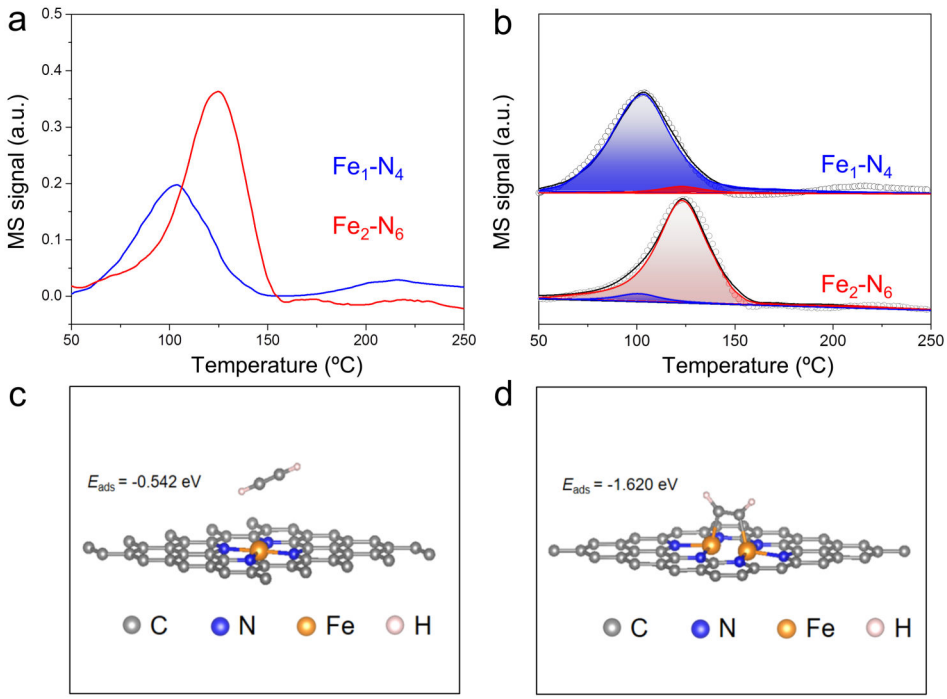

Supplementary Figure 26 | C_2H_2-TPD-MS profiles of Fe_1-N_4 and Fe_2-N_6. (**a**) Original C_2H_2-TPD-MS profiles of Fe_1-N_4 and Fe_2-N_6. (**b**) Peak fitting results. The adsorption configurations of acetylene on (**c**) Fe_1-N_4 and (**d**) Fe_2-N_6.

Note:

When we assume that one Fe site adsorbs one acetylene molecule, the purity of dual sites in the Fe_2N_6 sample was 91.4% based on the following equation.

Purity of dual sites = $S_{\text{dual sites}}$ / ($S_{\text{dual sites}}$ + $S_{\text{isolated sites}}$) = 10.6 / (10.6 + 1) = 91.4%

Actually, it is more rational that one isolated Fe site adsorb one acetylene molecule *via* an end-on mode, while a pair of dual Fe sites adsorb one acetylene molecule *via* a bidentate mode. In other words, for dual sites, one acetylene molecule corresponds to two Fe atoms. Thus, the purity of dual sites in the Fe_2-N_6 sample should be 95.5%, based on the following equation.

Purity of dual sites = 2 × $S_{\text{dual sites}}$ / (2 × $S_{\text{dual sites}}$ + $S_{\text{isolated sites}}$) = 2 × 10.6 / (2 × 10.6 + 1) = 95.5%

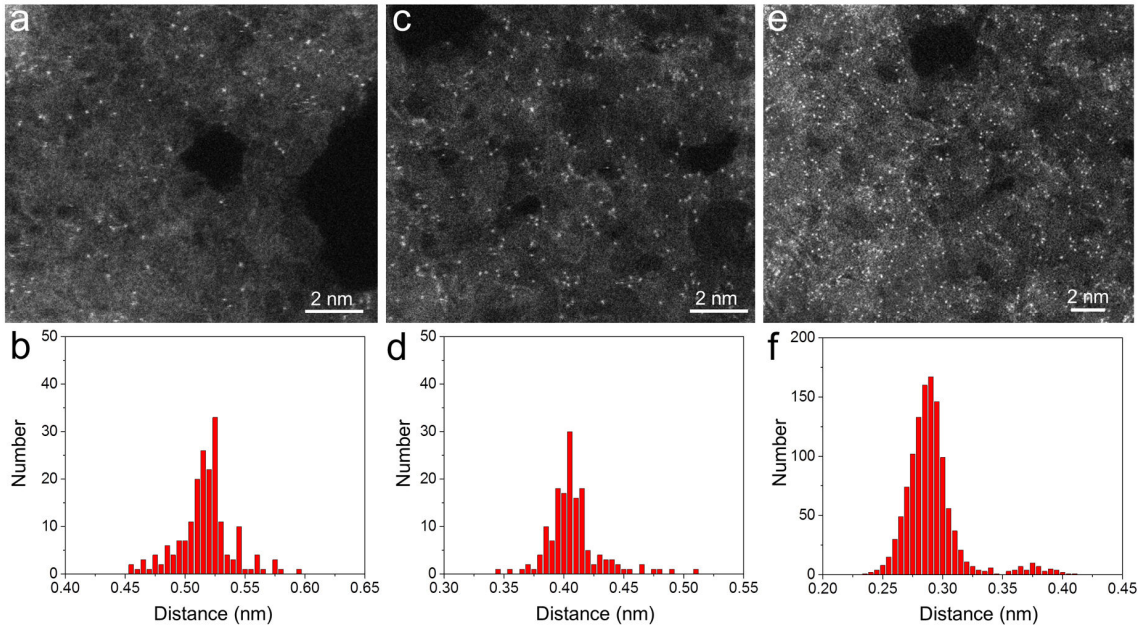

Supplementary Figure 27 | HAADF-STEM images of dual-atom Fe_2-N_x catalyst with different amounts of urea. HAADF-STEM images of dual-atom Fe_2-N_x catalyst by using (**a**) 10, (**c**) 50, and (**e**) 100 mg of urea. (**b, d, f**) Distance distribution between neighboring Fe atoms.

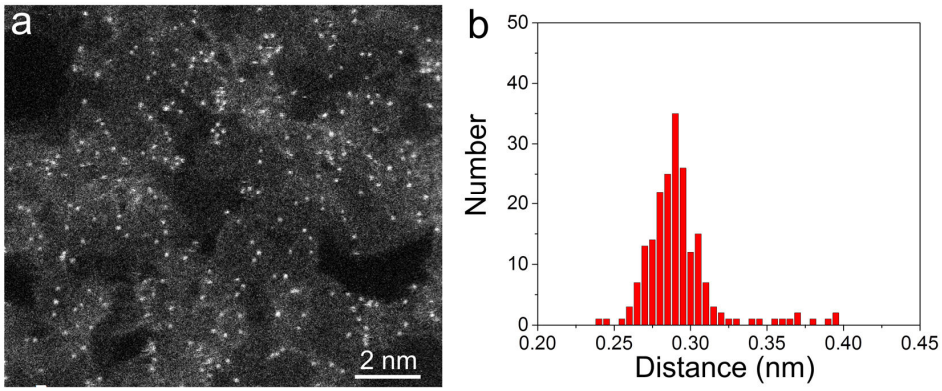

Supplementary Figure 28 | HAADF-STEM images of dual-atom Fe_2-N_x catalyst by using 120 mg of urea. (**a**) HAADF-STEM images of dual-atom Fe_2-N_x catalyst by using 120 mg of urea and (**b**) the corresponding distance distribution between neighboring Fe atoms.

Supplementary Table 3 | Comparison of synthesis conditions.

Sample	Coordination molecules	Usage of coordination molecules (mg)	Pyrolysis temperature (°C)	Fe contents (wt%)
Fe_1-N_4	No urea	/	700	0.32
Fe_2-N_6	Urea	10	700	0.55
Fe_2-N_6	Urea	30	700	0.96
Fe_2-N_6	Urea	50	700	1.32
Fe_2-N_6	Urea	100	700	2.36
Fe_2-N_6	Urea	120	700	2.37
Fe_2-N_6	Urea	50	500	1.62

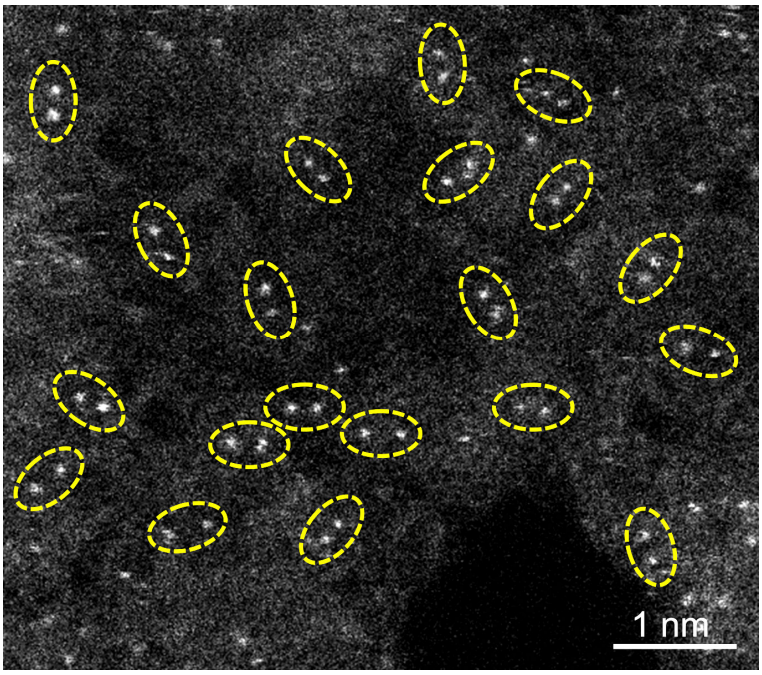

Supplementary Figure 29 | HAADF-STEM image of dual-atom Fe_2-N_x catalyst by using 50 mg of bidentate ligand of urea at a pyrolysis temperature of 500 °C.

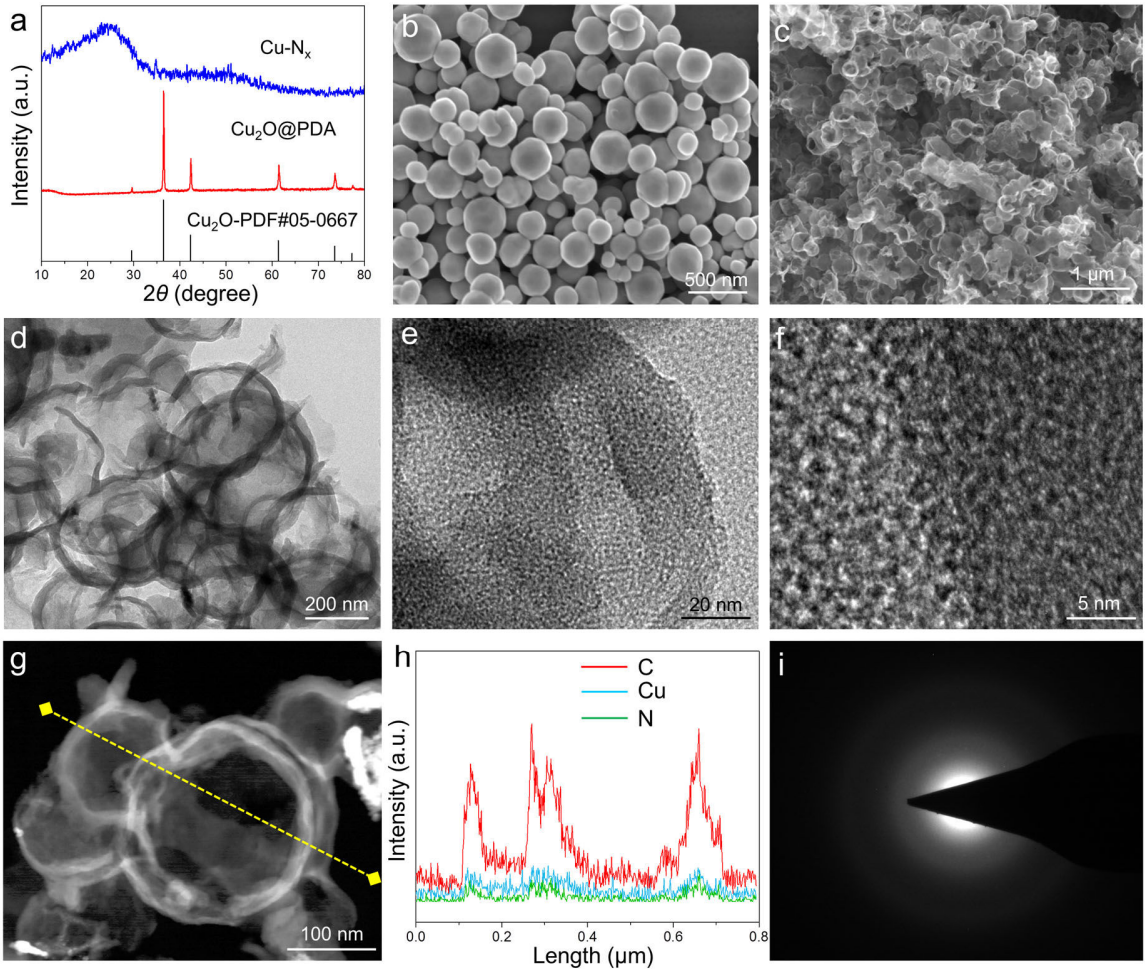

Supplementary Figure 30 | Structural analysis of neighboring Cu-N_x moieties. (**a**) XRD patterns of neighboring Cu-N_x moieties, Cu_2O@PDA, and the standard PDF#05-0667. (**b**) TEM image of Cu_2O nanoparticles. (**c**) SEM and (**d-f**) TEM images of neighboring Cu-N_x moieties at low and high magnifications. (**g**) HAADF-STEM image, (**h**) elemental line scan profiles, and (**i**) corresponding SAED result of neighboring Cu-N_x moieties.

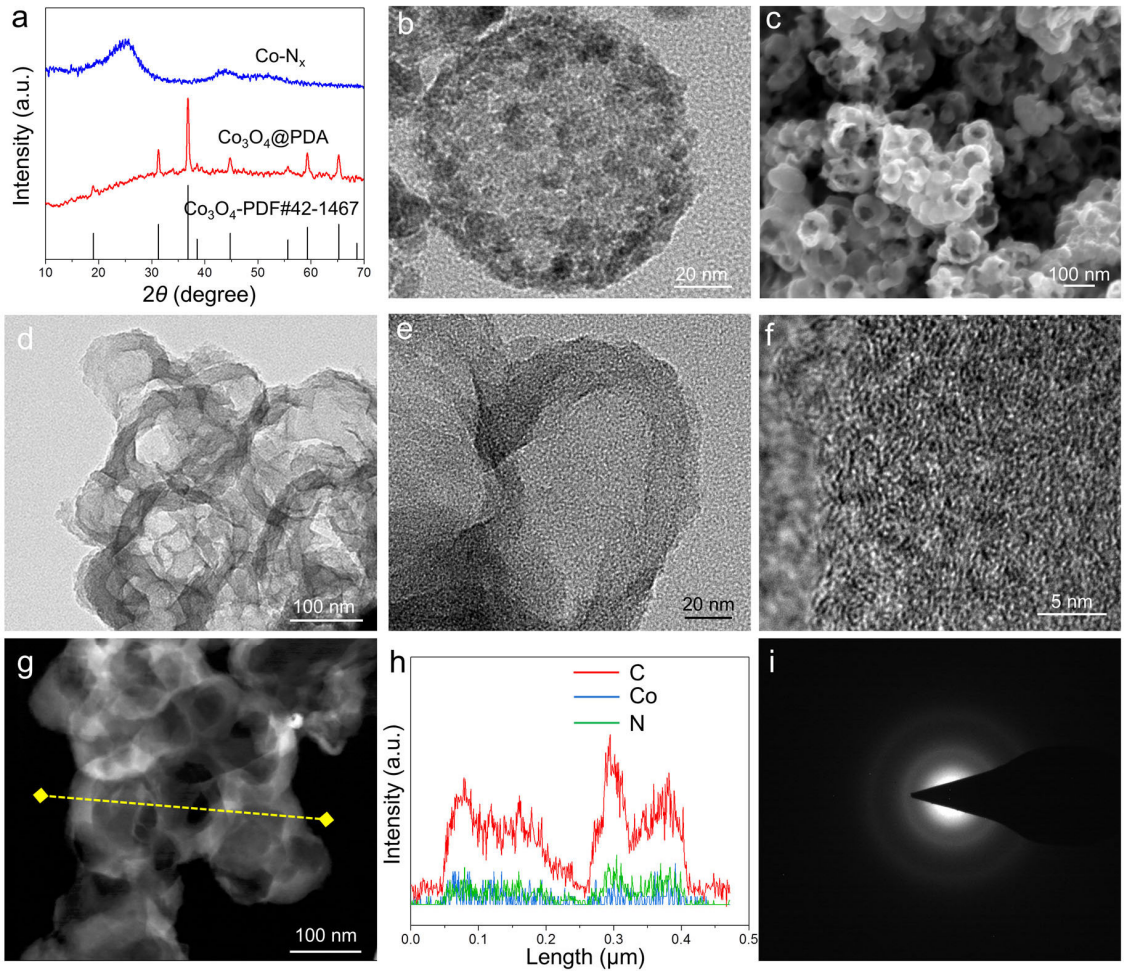

Supplementary Figure 31 | Structural analysis of neighboring Co-N_x moieties. (**a**) XRD patterns of neighboring Co-N_x moieties, Co_3O_4@PDA, and the standard PDF#42-1467. (**b**) TEM image of Co_3O_4 hollow sphere. (**c**) SEM and (**d-f**) TEM images of neighboring Co-N_x moieties at low and high magnifications. (**g**) HAADF-STEM image, (**h**) elemental line scan profiles, and (**i**) corresponding SAED result of neighboring Co-N_x moieties.

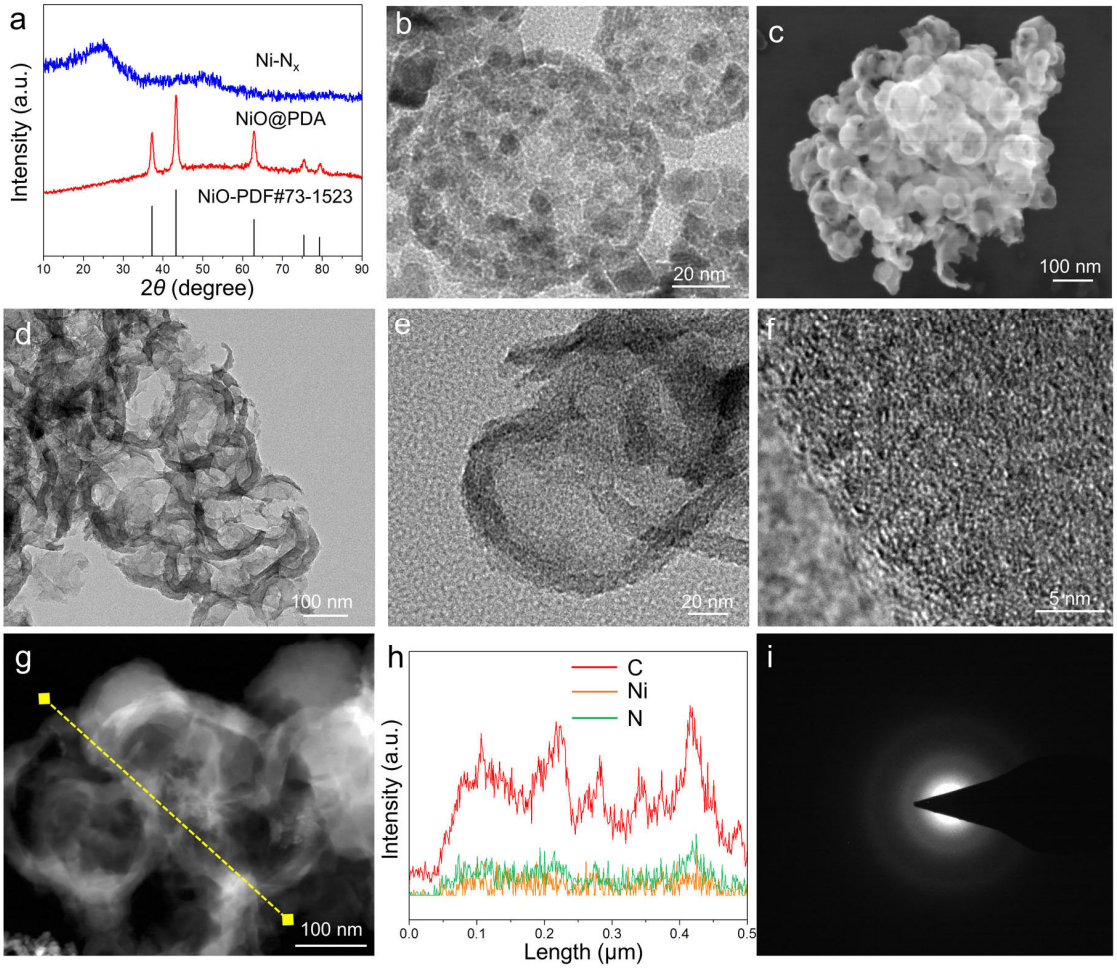

Supplementary Figure 32 | Structural analysis of neighboring Ni-N_x moieties. (a) XRD patterns of neighboring Ni-N_x moieties, NiO@PDA, and the standard PDF#42-1467. (b) TEM image of NiO hollow sphere. (c) SEM and (d-f) TEM images of neighboring Ni-N_x moieties at low and high magnifications. (g) HAADF-STEM image, (h) elemental line scan profiles, and (i) corresponding SAED result of neighboring Ni-N_x moieties.

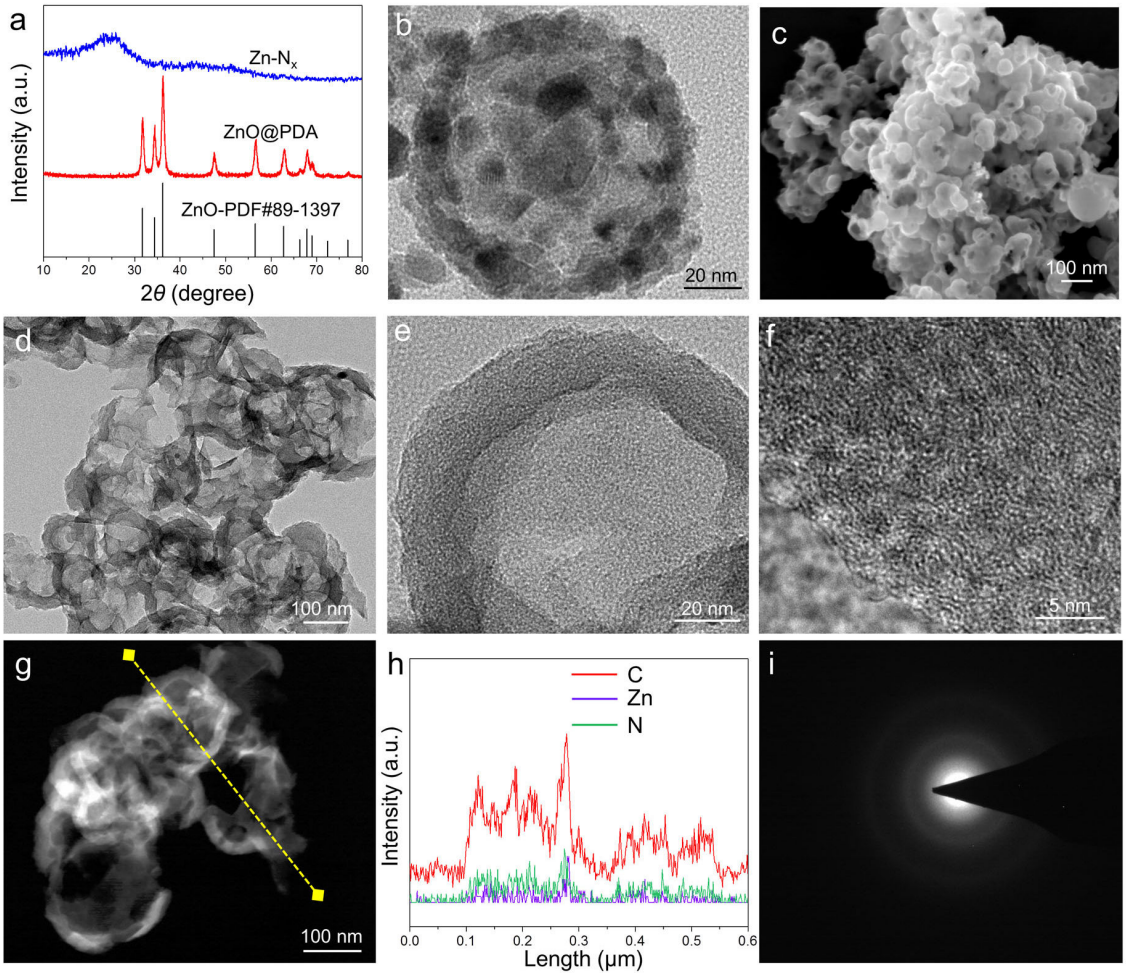

Supplementary Figure 33 | Structural analysis of neighboring Zn-N_x moieties. (**a**) XRD patterns of neighboring Zn-N_x moieties, ZnO@PDA, and the standard PDF#42-1467. (**b**) TEM image of ZnO hollow sphere. (**c**) SEM and (**d-f**) TEM images of neighboring Zn-N_x moieties at low and high magnifications. (**g**) HAADF-STEM image, (**h**) elemental line scan profiles, and (**i**) corresponding SAED result of neighboring Zn-N_x moieties.

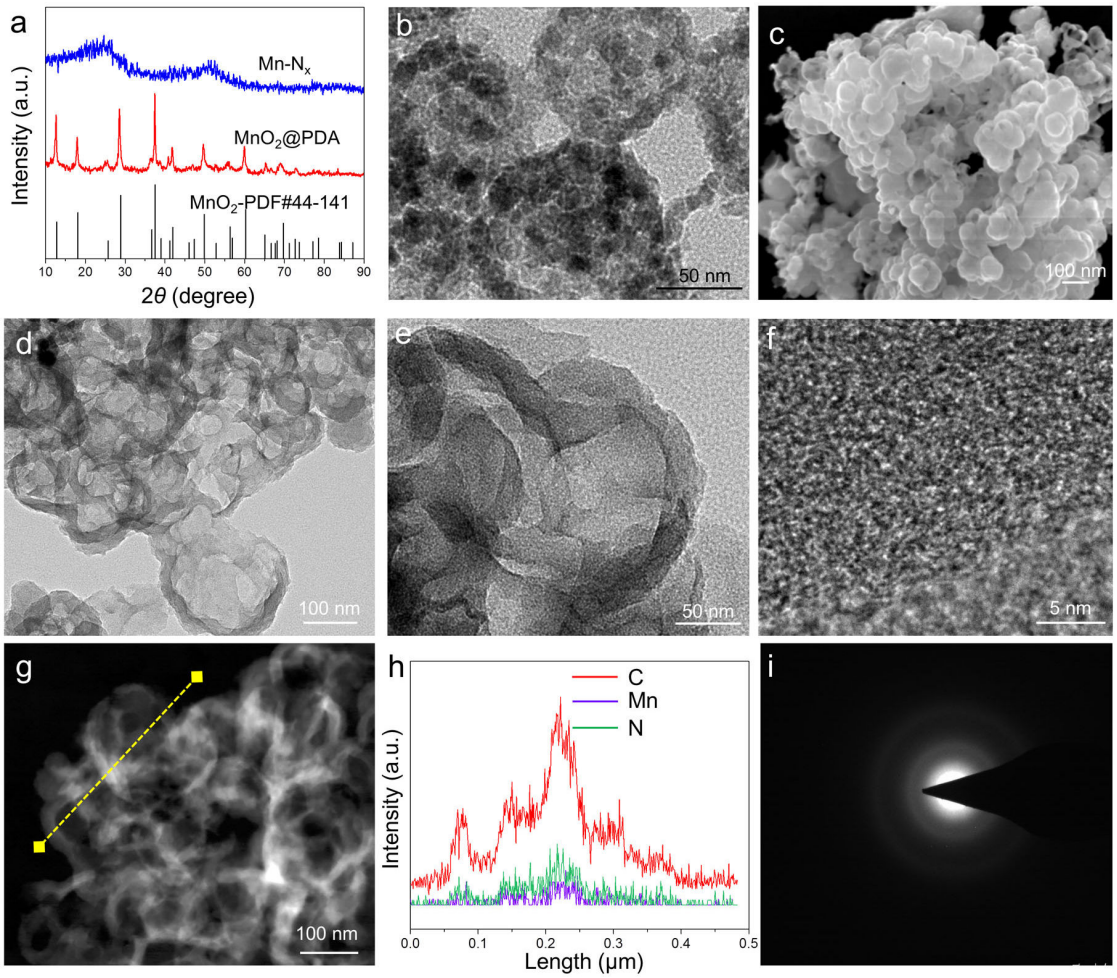

Supplementary Figure 34 | Structural analysis of neighboring Mn-N_x moieties. (**a**) XRD patterns of neighboring Mn-N_x moieties, MnO@PDA, and the standard PDF#42-1467. (**b**) TEM image of MnO hollow sphere. (**c**) SEM and (**d-f**) TEM images of neighboring Mn-N_x moieties at low and high magnifications. (**g**) HAADF-STEM image, (**h**) elemental line scan profiles, and (**i**) corresponding SAED result of neighboring Mn-N_x moieties.

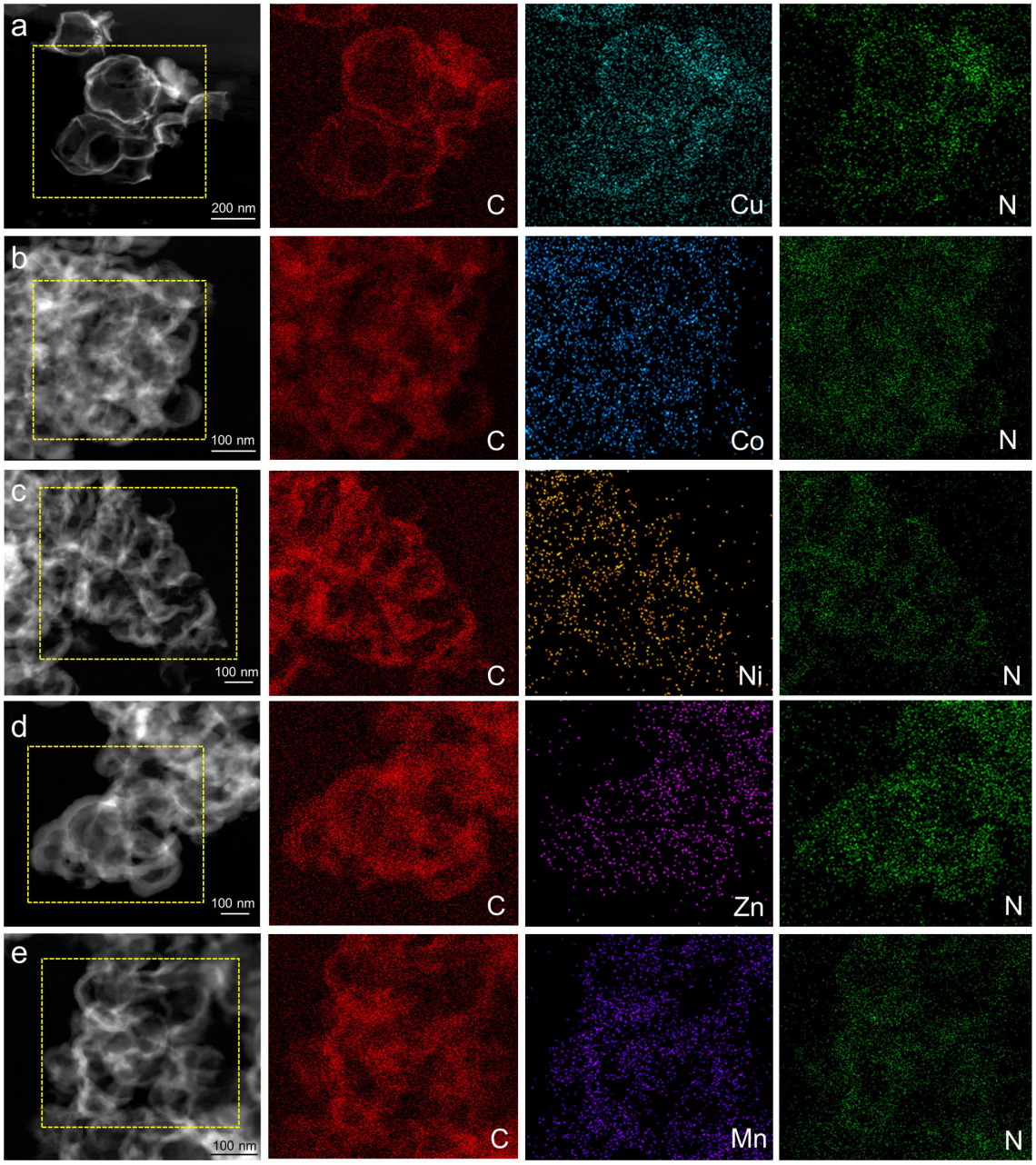

Supplementary Figure 35 | Structural analysis of different neighboring M-N_x moieties. HAADF-STEM image and EDS elemental mapping profiles of neighboring (**a**) Cu-N_x, (**b**) Co-N_x, (**c**) Ni-N_x, (**d**) Zn-N_x, and (**e**) Mn-N_x moieties.

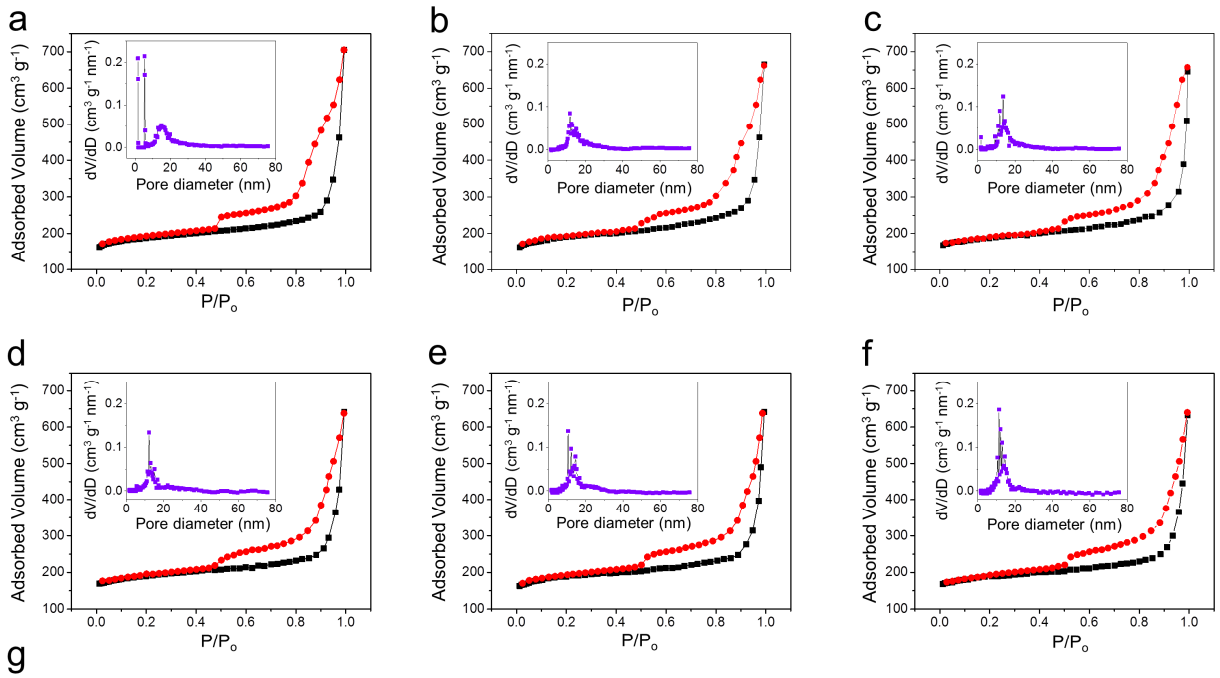

g

Samples	Items	No. 1	No. 2	No. 3	Average value	Standard deviation
Fe_1-N_4	Surface area (m^2 g^{-1})	521	509	514	515	5
Fe_2-N_6	Surface area (m^2 g^{-1})	507	518	515	513	5
Fe_1-N_4	Pore size (nm)	15.0	13.2	14.1	14.1	0.7
Fe_2-N_6	Pore size (nm)	13.6	14.5	14.9	14.3	0.5

Supplementary Figure 36 | Specific surface areas and pore size distribution. (**a-c**) N_2 adsorption/desorption isotherms and the corresponding pore size distribution of Fe_1-N_4 sample. (**d-f**) N_2 adsorption/desorption isotherms and the corresponding pore size distribution of Fe_2-N_6sample. (**g**) Average specific surface area and pore size for Fe_1-N_4 and Fe_2-N_6 samples.

Supplementary Table 4. Specific surface area and pore size distribution of Fe_1-N_4 and Fe_2-N_6.

Samples	Specific surface area (m^2 g^{-1})	pore size distribution (nm)
Fe_1-N_4	515 ± 5	14.1 ± 0.7
Fe_2-N_6	513 ± 5	14.3 ± 0.5

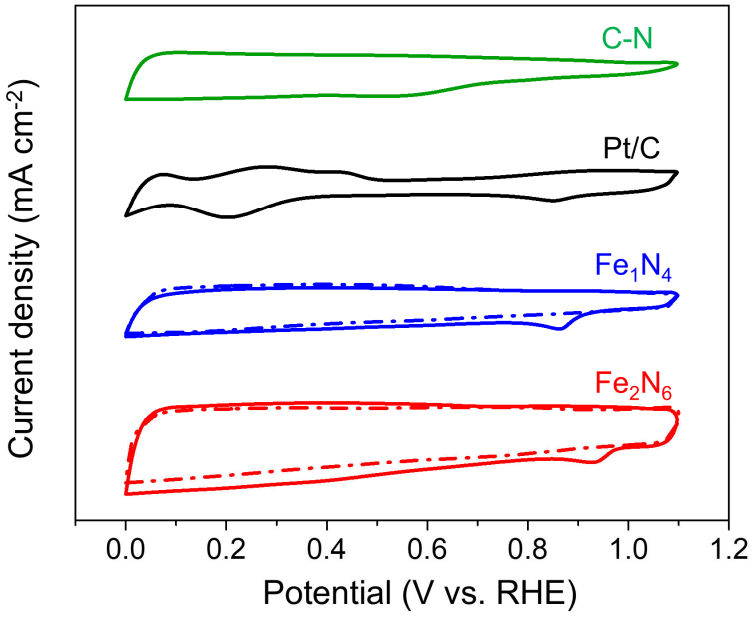

Supplementary Figure 37 | Cyclic voltammograms of catalysts in O_2 (solid lines) and N_2 (dashed lines) saturated 0.1 M KOH solution.

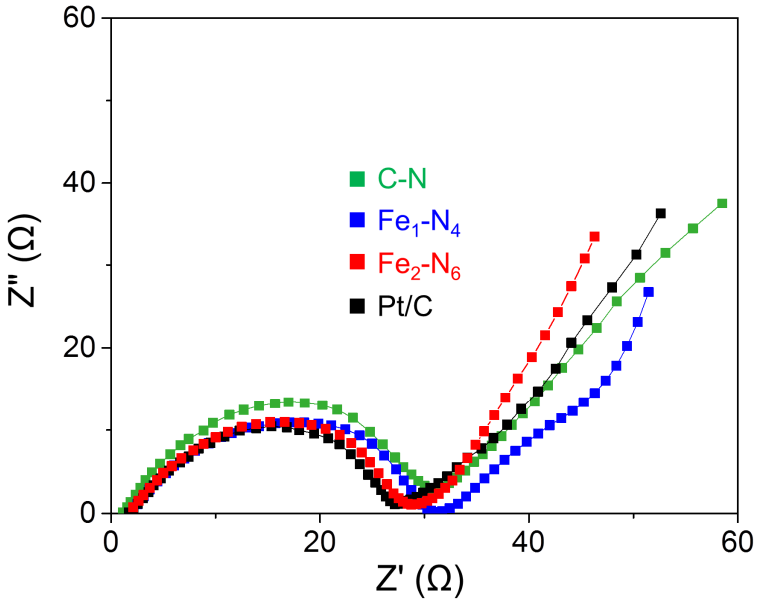

Supplementary Figure 38 | EIS spectra measured at 0.8 V vs. RHE for C-N, Fe_1-N_4, Fe_2-N_6 and commercial Pt/C.

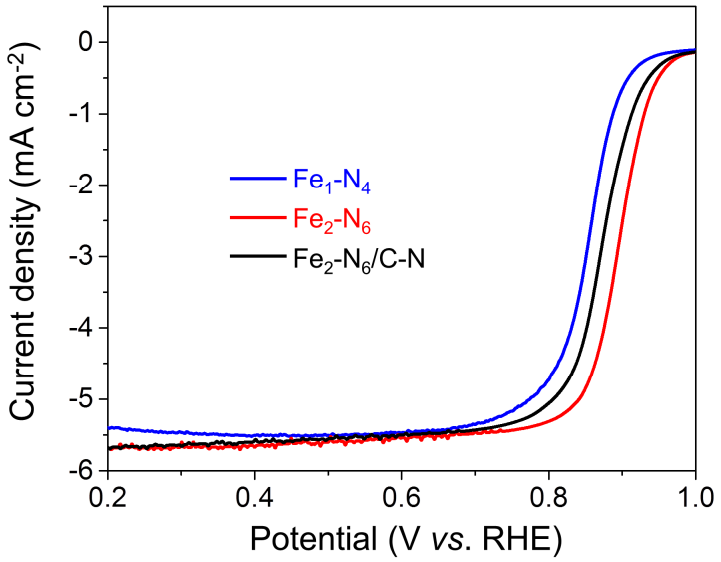

Supplementary Figure 39 | Linear sweep voltammetry curves of Fe_1-N_4, Fe_2-N_6, and Fe_2-N_6/C-N.

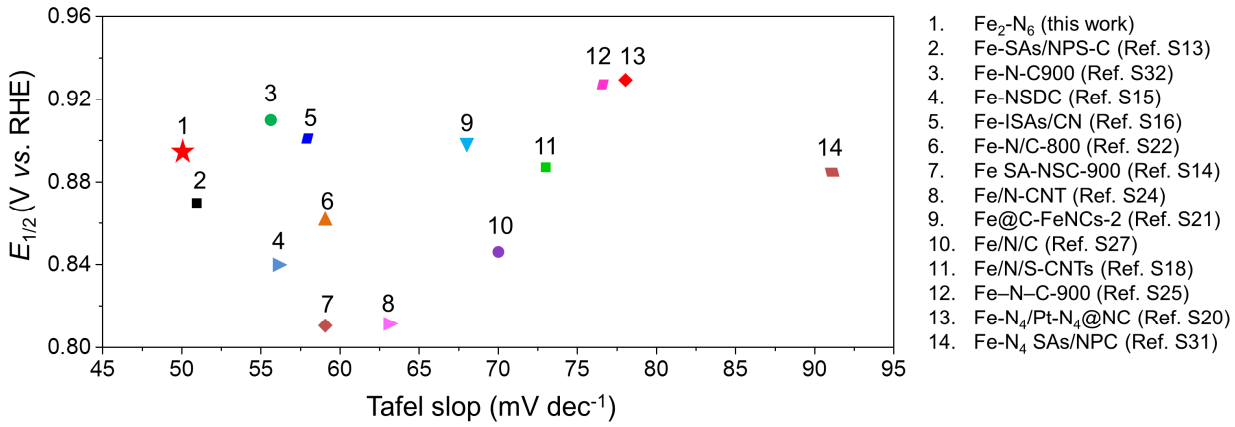

Supplementary Figure 40 | Comparison of ORR performance for Fe_2-N_6 with some reported catalysts in 0.1 M KOH solution.

Supplementary Table 5. Comparison of ORR performance for Fe_2-N_6 with some reported catalysts in 0.1 M KOH solution.

Catalysts	Loadings (mg/cm^2)	$E_{1/2}$ (V *vs*. RHE)	J_k (mA/cm^2)	Tafel ($mV\ dec^{-1}$)	Refs.
Fe_2-N_6	**0.25**	**0.894**	**29.4 at 0.85 V**	**50**	**This work**
Fe-SAs/NPS-C	-	0.87	34.6 at 0.85 V	51	S1
Fe SA-NSC-900	0.10	~0.86	-	59	S2
Fe-NSDC	0.10	0.84	-	56	S3
Fe-ISAs/CN	0.51	0.90	37.83 at 0.85 V	58	S4
S-Fe/N/C	0.16	0.839	-	-	S5
Fe/N/S-CNTs	0.51	0.887		73	S6
Fe-N/P-C-700	~3.0	0.867	24.49	-	S7
Fe-N_4/Pt-N_4@NC	-	0.93	27.2 at 0.85 V	78	S8
Fe@C-FeNCs-2	0.70	0.899	41.6 at 0.8 V	68	S9
Fe-N/C-800	0.079	0.81	0.4 at 0.9 V	59	S10
Fe-NC SAC	-	0.90	-	48	S11
Fe/N-CNT	~0.20	0.81	-	63	S12
Fe–N–C-900	0.20	0.927	~28 at 0.85 V	76.6	S13
meso-Fe-N-C	0.40	0.846	4.696 at 0.85 V	-	S14
Fe/N/C	0.06	0.845	-	70	S15
S,N-Fe/N/C-CNT	0.60	0.850	7.350 at 0.85 V	-	S16
Fe–N/C-155	0.245	0.850	5.86 at 0.90 V	-	S17
FeN_x-PNC	0.14	0.86	-	-	S18
Fe-N_4 SAs/NPC	2.0	0.885	7.47 at 0.85 V	91	S10
Fe–N–C900	0.6	0.91	-	55.45	S20

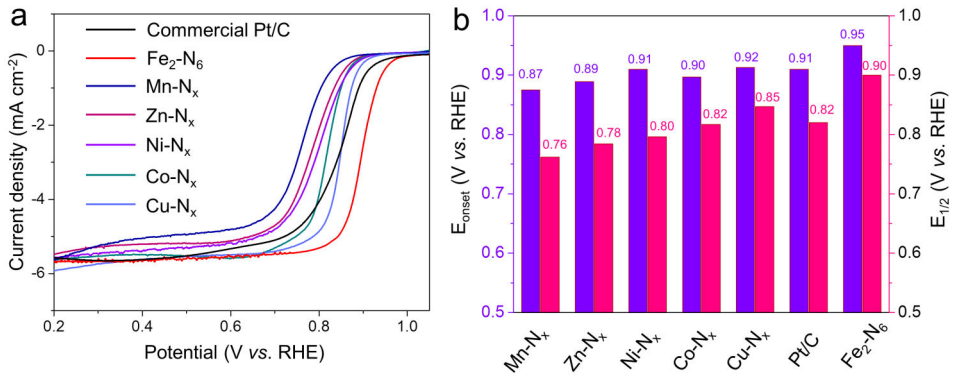

Supplementary Figure 41 | Comparison in ORR activities of different neighboring M-N_x (M = Cu, Co, Ni, Zn, and Mn) moieties. (**a**) LSV curves and (**b**) corresponding electrochemical values of M-N_x (M = Cu, Co, Ni, Zn, and Mn), Fe_2-N_6, and commercial Pt/C. Here, the obtained values of onset points and half-wave potential for M-N_x (M = Cu, Co, Ni, Zn, and Mn) moieties were lower than Fe-N_x species.

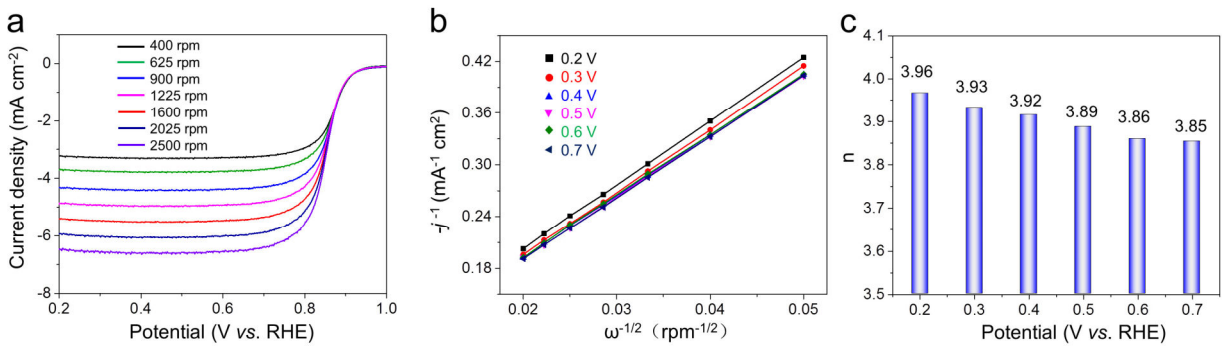

Supplementary Figure 42 | Electrochemical kinetics of Fe_1-N_4. (**a**) LSV curves of Fe_1-N_4 at various rotation rates. (**b**) The corresponding Koutecky-Levich plots. (**c**) The calculated n value at different potentials for Fe_1-N_4.

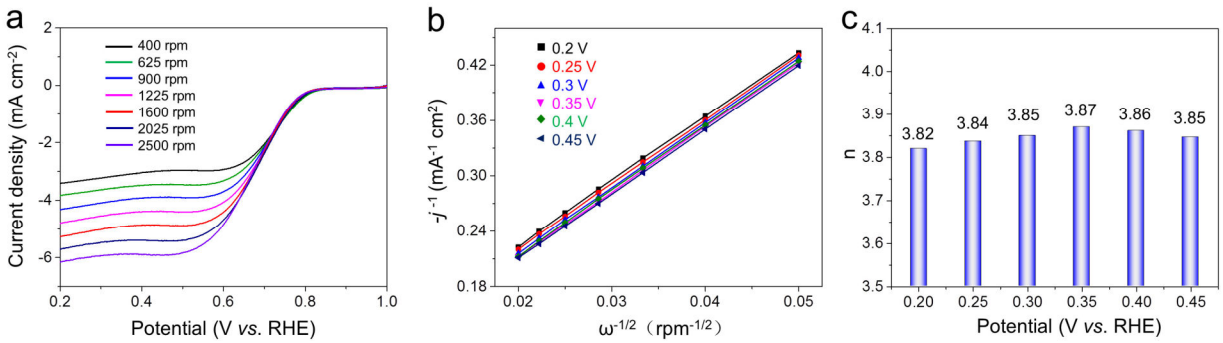

Supplementary Figure 43 | Electrochemical kinetics of C-N sample. (**a**) LSV curves of carbon matrix sample at various rotation rates. (**b**) The corresponding Koutecky-Levich plots. (**c**) The calculated n value at different potentials for the carbon matrix.

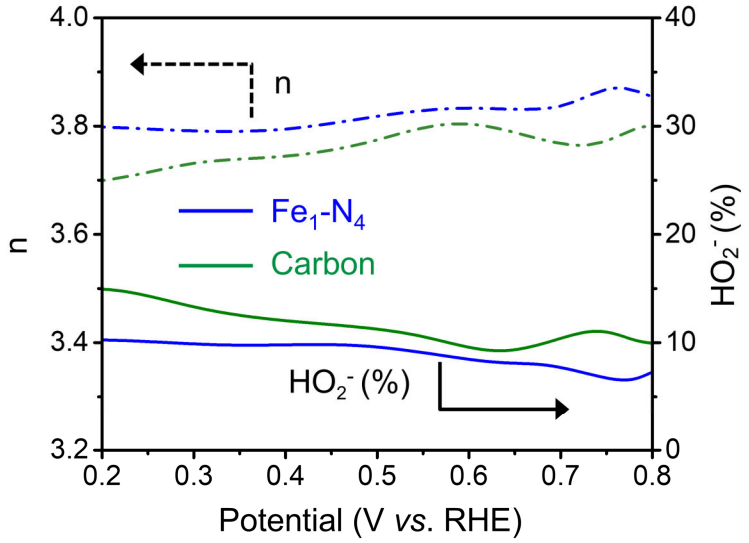

Supplementary Figure 44 | Electron transfer number (n) (top) and HO_2^- yield (bottom) of Fe_1-N_4 and carbon matrix. The n value of Fe_1-N_4 is about 3.79 - 3.87, and the n value for carbon is about 3.69 - 3.81.

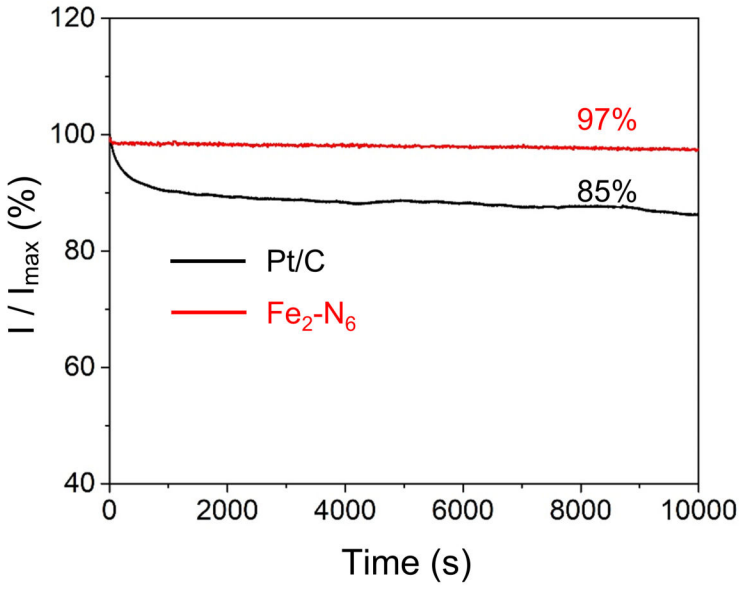

Supplementary Figure 45 | Current−time chronoamperometric responses of Fe_2-N_6 compared with those of Pt/C.

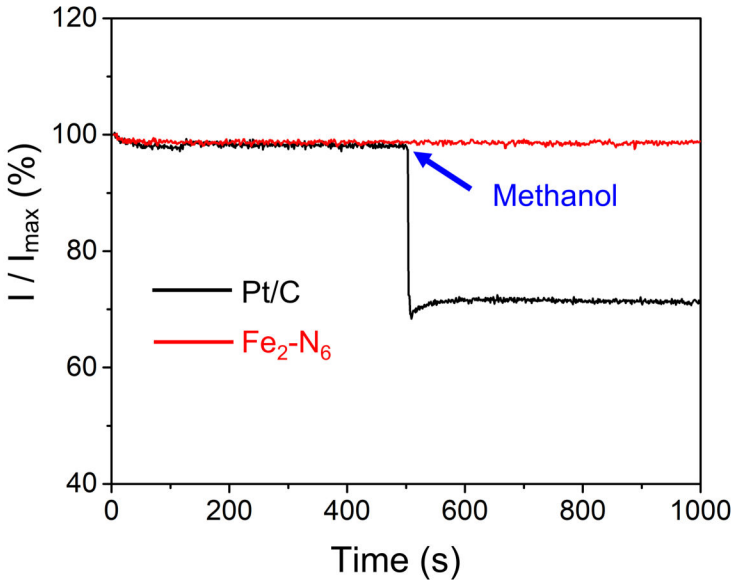

Supplementary Figure 46 | Tolerance to methanol of Fe_2-N_6 compared with those of Pt/C (20%) electrocatalyst. The arrow indicates the injection of 2 mL of methanol.

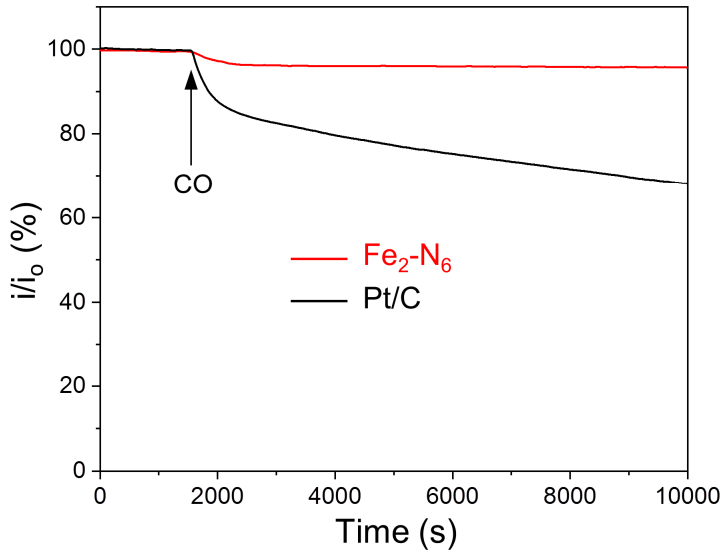

Supplementary Figure 47 | Tolerance to carbon monoxide of Fe_2-N_6 compared with Pt/C electrocatalyst. CO-poison effect on the i-t chronoamperometric response for Fe_2-N_6, Fe_1-N_4 and Pt/C electrodes in presence of O_2. The arrow indicates the addition of ~10% (volume/volume vs O_2) CO gas into the O_2-saturated 0.1 M KOH electrochemical cell. And i_o means the initial current.

Supplementary Table 6. Quantitative analysis of Supplementary Figure 37. Quantitative comparison of CO tolerance between Fe_2-N_6 and Pt/C.

Catalysts	i(t)/i_0			$\Delta i/i_0$[d]	τ_1 (s)[e]	τ_2 (s)[f]
	1550 s[a]	3000 s[b]	10000 s[c]			
Fe_2-N_6	99.77%	96.16%	95.65%	4.12%	2834	53837
Pt/C	99.37%	82.52%	68.09%	31.28%	1964	8815

[a]Time when CO was added.
[b]Time after when the current of Fe_2-N_6 became stable.
[c]End time.
[d]The variation of current between 1550 s and 10000 s normalized by initial current.
[e]Mean life time based on the parameters of i_1 = i(1550 s), i_2 = i(10000 s).
[f]Mean life time based on the parameters of i_1 = i(3000 s), i_2 = i(10000 s).

Notes:

As shown in Supplementary Figure 34, after a relatively rapid deactivation process, the current of Fe_2-N_6 remained almost unchanged even when the reaction time was extended to 10000 s (Fig. R3b). As shown in the above table, the activity loss of Pt/C was 31.28%, which was 7.6 times more than that (4.12%) of Fe_2-N_6 after 10000 s. Since the operation time was long enough to quantify the stability, we calculated its deactivation coefficient (k_d) and mean life time (τ) based on assuming first-order deactivation kinetics. As such, the values of k_d and τ are obtained according to equations 1 and 2. In equation 1, i_1 and i_2 represent the initial current and the final current, respectively, while t represents the time interval between the initial and final states.

$$k_d\, t = \ln\left[(1 - i_2)/i_2\right] - \ln\left[(1 - i_1)/i_1\right] \quad (1)$$

$$\tau = 1/k_d \quad (2)$$

When we used the current upon CO addition, i(1550 s), as the initial current, the mean lifetime of Fe_2-N_6 was calculated as 2834 s, which was 1.44 times longer than that (1964 s) of Pt/C. Considering that the current of Fe_2-N_6 became stable after 3000 s, we further took the

current at this time, i(3000 s), as the initial current. Under this circumstance, the mean life time of Fe_2-N_6 was calculated as 53837 s, which was 6.11 times longer than that (8815 s) of Pt/C. Overall, the CO tolerance of Fe_2-N_6 was significantly better than that of Pt/C. Moreover, the advantage of Fe_2-N_6 became more prominent with the extension of reaction time.

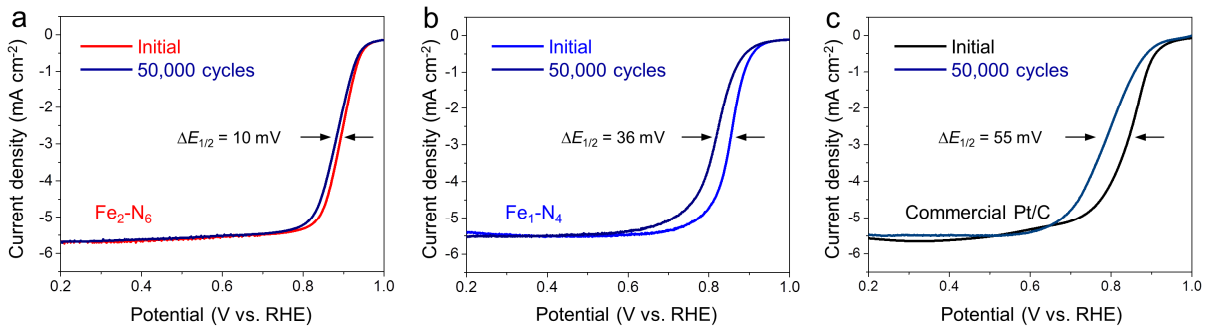

Supplementary Figure 48 | ORR polarization curves before and after 50,000 cycles. ORR polarization curves before and after 50,000 cycles over (**a**) Fe_2-N_6., (**b**) Fe_1-N_4, and (**c**) commercial Pt/C.

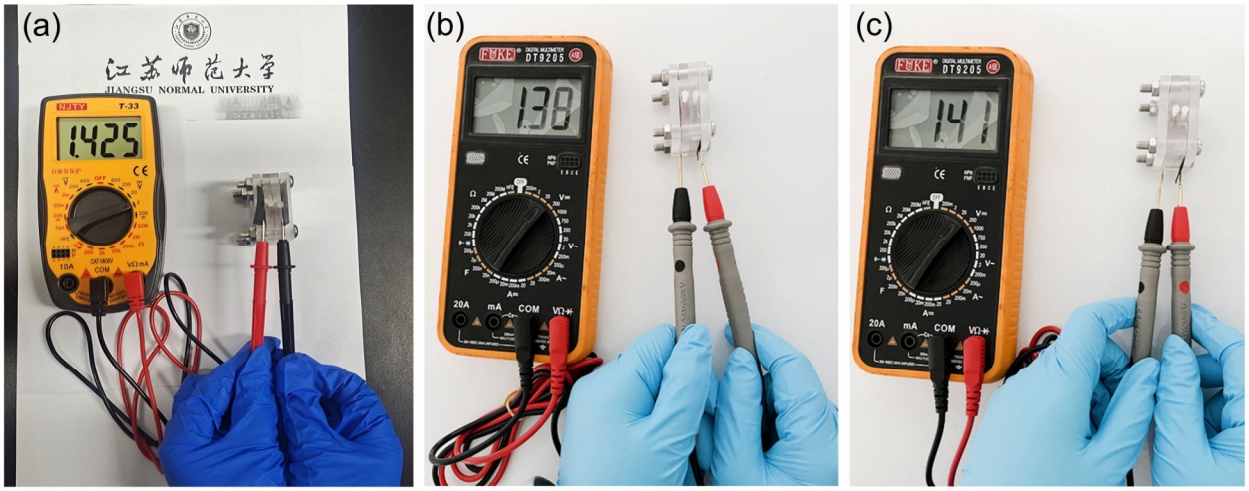

Supplementary Figure 49 | Photos. Photo showing the voltage of a single Zn-air battery with (**a**) Fe_2-N_6 , (**b**) Fe_1-N_4 and (**c**) commercial Pt/C as the cathodic catalyst.

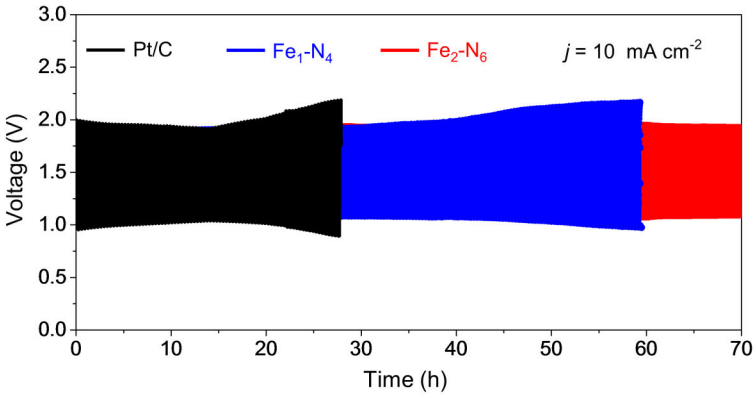

Supplementary Figure 50 | Long-term cycling performance of commercial Pt/C, Fe_1-N_4 and Fe_2-N_6 samples.

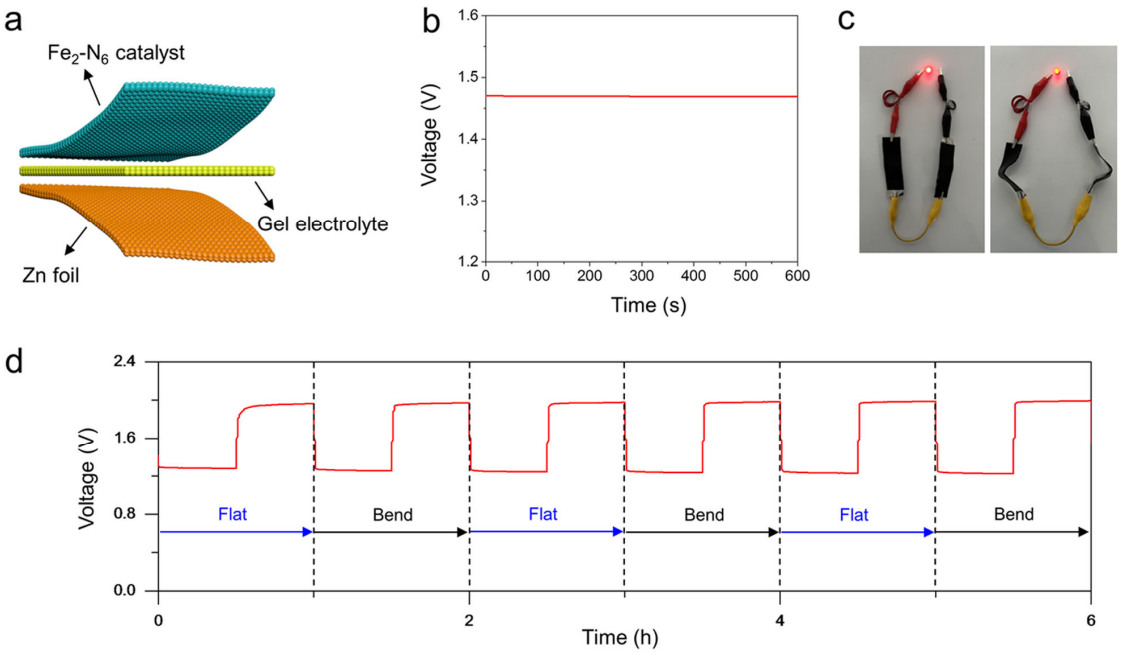

Supplementary Figure 51 | Flexible Zn-air batteries with Fe_2-N_6 catalyst as a cathode. (**a**) Schematic image of the flexible Zn-air battery with Fe_2-N_6 catalyst and Zn foil as air cathode and anode; (**b**) Open-circuit voltage-time curve for the assembled Zn-air battery; (**c**) Optical pictures of a red LED that lit up by two assembled Zn-air batteries with Fe_2-N_6 catalyst as cathode; (**d**) Charge-discharge curves of Zn-air battery with Fe_2-N_6 cathode at alternatively flat and bend states.

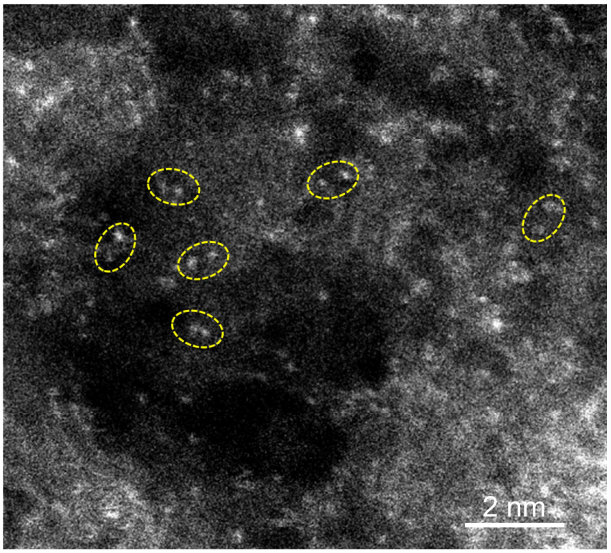

Supplementary Figure 52 | HAADF-STEM image of prepared Fe_2-N_6 catalyst after 50,000 times cycling.

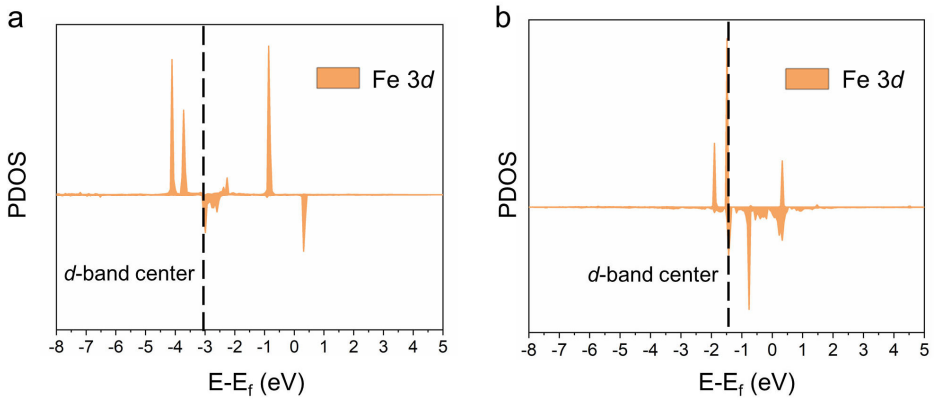

Supplementary Figure 53 | PDOS analysis. PDOS for Fe 3*d* orbitals of (**a**) Fe_1-N_4 and (**b**) Fe_2-N_6.

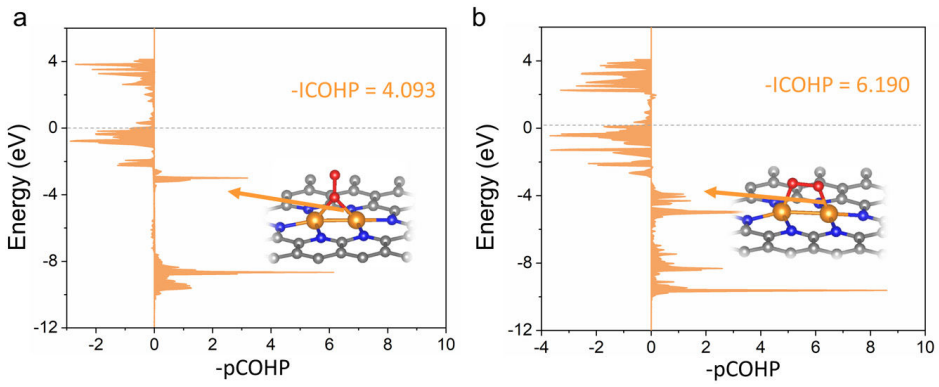

Supplementary Figure 54 | Projected COHP analysis. Projected COHP of (**a**) Fe_2-N_6-O_2-ver and (**b**) Fe_2-N_6-O_2-par. The Fe_2-N_6-O_2-ver and Fe_2-N_6-O_2-par have two Fe-O bonds.

References

S1. Chen, Y. *et al.* Enhanced oxygen reduction with single-atomic-site iron catalysts for a zinc-air battery and hydrogen-air fuel cell. *Nat. Commun.* **9**, 5422 (2018).

S2. Wang, M. *et al.* Atomically Dispersed Fe–Heteroatom (N, S) Bridge Sites Anchored on Carbon Nanosheets for Promoting Oxygen Reduction Reaction. *ACS Energy Lett.* **6**, 379-386 (2021).

S3. Zhang, J. *et al.* Single Fe Atom on Hierarchically Porous S, N-Codoped Nanocarbon Derived from Porphyra Enable Boosted Oxygen Catalysis for Rechargeable Zn-Air Batteries. *Small* **15**, 1900307 (2019).

S4. Chen, Y. *et al.* Isolated Single Iron Atoms Anchored on N-Doped Porous Carbon as an Efficient Electrocatalyst for the Oxygen Reduction Reaction. *Angew. Chem. Int. Ed.* **56**, 6937-6941 (2017).

S5. Hu, K., Tao, L., Liu, D., Huo, J. & Wang, S. Sulfur-Doped Fe/N/C Nanosheets as Highly Efficient Electrocatalysts for Oxygen Reduction Reaction. *ACS Appl. Mater. Interfaces* **8**, 19379-19385 (2016).

S6. Jin, H. *et al.* In situ derived Fe/N/S-codoped carbon nanotubes from ZIF-8 crystals as efficient electrocatalysts for the oxygen reduction reaction and zinc–air batteries. *J. Mater. Chem. A* **6**, 20093-20099 (2018).

S7. Yuan, K. *et al.* Boosting Oxygen Reduction of Single Iron Active Sites via Geometric and Electronic Engineering: Nitrogen and Phosphorus Dual Coordination. *J. Am. Chem. Soc.* **142**, 2404-2412 (2020).

S8. Han, A. *et al.* An Adjacent Atomic Platinum Site Enables Single-Atom Iron with High Oxygen Reduction Reaction Performance. *Angew. Chem. Int. Ed.* **60**, 19262-19271 (2021).

S9. Jiang, W.-J. *et al.* Understanding the High Activity of Fe–N–C Electrocatalysts in Oxygen Reduction: Fe/Fe_3C Nanoparticles Boost the Activity of Fe–Nx. *J. Am. Chem. Soc.* **138**, 3570-3578 (2016).

S10. Niu, W. *et al.* Mesoporous N-Doped Carbons Prepared with Thermally Removable Nanoparticle Templates: An Efficient Electrocatalyst for Oxygen Reduction Reaction. *J. Am. Chem. Soc.* **137**, 5555-5562 (2015).

S11. Zhao, L. *et al.* Cascade anchoring strategy for general mass production of high-loading single-atomic metal-nitrogen catalysts. *Nat. Commun.* **10**, 1278 (2019).

S12. Liu, Y., Jiang, H., Zhu, Y., Yang, X. & Li, C. Transition metals (Fe, Co, and Ni) encapsulated in nitrogen-doped carbon nanotubes as bi-functional catalysts for oxygen electrode reactions. *J. Mater. Chem. A* **4**, 1694-1701 (2016).

S13. Zhu, C. *et al.* Hierarchically Porous M–N–C (M = Co and Fe) Single-Atom Electrocatalysts with Robust MNx Active Moieties Enable Enhanced ORR Performance. *Adv. Energy Mater.* **8**, 1801956 (2018).

S14. Zhou, Y. *et al.* Atomic Fe Dispersed Hierarchical Mesoporous Fe–N–C Nanostructures for an Efficient Oxygen Reduction Reaction. *ACS Catal.* **11**, 74-81 (2021).

S15. Wu, Y., Nagata, S. & Nabae, Y. Genuine four-electron oxygen reduction over precious-metal-free catalyst in alkaline media. *Electrochim. Acta* **319**, 382-389 (2019).

S16. Chen, P. *et al.* Atomically Dispersed Iron–Nitrogen Species as Electrocatalysts for Bifunctional Oxygen Evolution and Reduction Reactions. *Angew. Chem. Int. Ed.* **56**, 610-614 (2017).

S17. Ye, G. *et al.* Cage-confinement of gas-phase ferrocene in zeolitic imidazolate frameworks to synthesize high-loading and atomically dispersed Fe–N codoped carbon for efficient oxygen reduction reaction. *J. Mater. Chem. A* **7**, 16508-16515 (2019).

S18. Ma, L. *et al.* Single-Site Active Iron-Based Bifunctional Oxygen Catalyst for a Compressible and Rechargeable Zinc–Air Battery. *ACS Nano* **12**, 1949-1958 (2018).

S19. Pan, Y. *et al.* A Bimetallic Zn/Fe Polyphthalocyanine-Derived Single-Atom $Fe-N_4$ Catalytic Site:A Superior Trifunctional Catalyst for Overall Water Splitting and Zn–Air Batteries. *Angew. Chem. Int. Ed.* **57**,

8614-8618 (2018).

S20. Lyu, D. *et al.* Ultra-high surface area graphitic Fe-N-C nanospheres with single-atom iron sites as highly efficient non-precious metal bifunctional catalysts towards oxygen redox reactions. *J. Catal.* **368**, 279-290 (2018).